

THE GREENHOUSE EFFECT IN BURIED GALACTIC NUCLEI AND THE RESONANT HCN VIBRATIONAL EMISSION

EDUARDO GONZÁLEZ-ALFONSO¹ AND KAZUSHI SAKAMOTO²

¹*Universidad de Alcalá, Departamento de Física y Matemáticas, Campus Universitario, E-28871 Alcalá de Henares, Madrid, Spain*

²*Academia Sinica, Institute of Astronomy and Astrophysics, Taipei 10617, Taiwan*

ABSTRACT

Recent interferometric observations have shown bright HCN emission from the $\nu_2 = 1$ vibrational state arising in buried nuclear regions of galaxies, indicating an efficient pumping of the $\nu_2 = 1$ state through absorption of $14 \mu\text{m}$ continuum photons. We have modeled the continuum and HCN vibrational line emission in these regions, characterized by high column densities of dust and high luminosities, with a spherically symmetric approach, simulating both a central heating source (AGN) and a compact nuclear starburst (SB). We find that when the H_2 columns become very high, $N_{\text{H}_2} \gtrsim 10^{25} \text{ cm}^{-2}$, trapping of continuum photons within the nuclear region dramatically enhances the dust temperature (T_{dust}) in the inner regions, even though the predicted spectral energy distribution as seen from outside becomes relatively cold. The models thus predict bright continuum at millimeter wavelengths for luminosity surface brightness (averaged over the model source) of $\sim 10^8 L_{\odot} \text{ pc}^{-2}$. This *greenhouse* effect significantly enhances the mean mid-infrared intensity within the dusty volume, populating the $\nu_2 = 1$ state to the extent that the HCN vibrational lines become optically thick. AGN models yield higher T_{dust} in the inner regions and higher peak (sub)millimeter continuum brightness than SB models, but similar HCN vibrational $J = 3-2$ and $4-3$ emission owing to both optical depth effects and a moderate impact of high T_{dust} on these low- J lines. The observed HCN vibrational emission in several galaxies can be accounted for with a HCN abundance of $\sim 10^{-6}$ (relative to H_2) and luminosity surface brightness in the range $(0.5-2) \times 10^8 L_{\odot} \text{ pc}^{-2}$, predicting a far-infrared photosphere with $T_{\text{dust}} \sim 80-150 \text{ K}$ —in agreement with the values inferred from far-infrared molecular absorption.

Keywords: galaxies: ISM — galaxies: evolution — infrared: galaxies — millimeter: galaxies — line: formation

1. INTRODUCTION

Buried galactic nuclei (hereafter BGN) are compact ($\lesssim 100$ pc) nuclear regions in galaxies with both high gas column densities ($\gtrsim 10^{24}$ H₂ cm⁻²) and high luminosity surface brightnesses ($\gtrsim 10^7$ L_⊙ pc⁻²). Both starbursts and buried, accreting supermassive black holes (i.e., active galactic nuclei, AGNs) are suspected to power BGNs, although the dominant luminosity sources in individual nuclei and in the entire BGN population are unclear and under debate. In the local Universe, they are mostly observed in (Ultra)-Luminous Infrared Galaxies, (U)LIRGs, and when present they contribute significantly to the high luminosities of these galaxies (Soifer et al. 2000). Obscured nuclei may be formed through the loss of angular momentum of the gas associated with a merger event or a strong bar (e.g. Hopkins et al. 2008), or via dissipative contraction of gas-rich disks that become unstable due to cold inflows (Dekel & Burkert 2014). All these mechanisms involve neutral inflows that are indeed observed in some (U)LIRGs via inverse P-Cygni profiles or redshifted absorption in [O I] 63 μm and/or ground-state OH (González-Alfonso et al. 2012, 2017; Falstad et al. 2015, 2017). At higher redshifts, mergers and cold inflows are probably more common than locally, and so are the formation of obscured nuclei; they have been identified from the high infrared to X-ray luminosity ratio and their negligible emission at optical wavelengths (Chang et al. 2017), though their statistical significance is still not well addressed.

Given the extreme extinction that characterize BGNs, the most promising way to identify and give insight into their physics is through continuum studies with high angular resolution at millimeter wavelengths and with molecular spectroscopy from the infrared to centimeter wavelengths. Interferometric observations have measured 0.8–3 mm continuum brightness temperatures of hundreds of Kelvin at the scale of a few tens of parsecs or less in the nuclei of some (U)LIRGs (e.g., Sakamoto et al. 2013, 2017; Aalto et al. 2019). Attributing the continuum to thermal emission from dust (as supported by radio spectral energy distribution), the strongly peaked emission suggests high luminosity surface densities in the nuclei. As a guide, a 100 K blackbody sphere has a luminosity surface density of $L_{\text{IR}}/(\pi R^2) \approx 6 \times 10^7$ L_⊙ pc⁻². (We will see later the effect of gas and dust covering such a source.) These nuclei also need to have the high column densities of BGNs in order for dust to have a significant optical depth that can explain these high brightness temperatures. At far-infrared (far-IR) wavelengths, BGNs are characterized by high-lying (i.e., lower-level energy $E_{\text{low}} \gtrsim 300$ K) absorption lines of various molecular species against the continuum—usually associated with a strong [C II] deficit (e.g. González-Alfonso et al. 2015, and references therein). The OH 65 μm doublet (with $E_{\text{low}} \approx 300$ K), observed in a number of (U)LIRGs with

Herschel/PACS, has been used as a far-IR signature of these regions; however, not all sources that show deep OH 65 μm absorption are similar as they span an important range in column densities and molecular excitation, with a threshold of $N_{\text{H}} \sim 10^{24}$ cm⁻² above which the doublet is saturated.

To overcome the curtain of obscuring dust, the observation of high-lying molecular lines in emission at (sub)millimeter and centimeter wavelengths also provide high angular resolution and are thus highly useful. Of special interest are the vibrationally excited HCN ν_2 and HC₃N ν_7 and ν_6 lines. Probably due to the combination of high columns, which protect these species from photoionization, and high temperatures (Harada et al. 2010), cyanopolynes attain high abundances and their vibrational lines are prominent in these regions in spite of their involved high-energy levels (> 1000 K for HCN). Following the first extragalactic detection of the HCN $\nu_2 = 1^f J = 3-2$ and $J = 4-3$ lines in the prototypical BGN NGC 4418 (Sakamoto et al. 2010), the HCN vibrational lines have been detected and imaged in a number of BGNs (Aalto et al. 2015a,b; Martín et al. 2016; Imanishi et al. 2016a,b; Falstad et al. 2018), indicating a very efficient pumping of the vibrational states through absorption of 14 μm continuum photons—the wavelength of the vibrational band detected in strong absorption towards the same objects by Lahuis et al. (2007).

The HCN vibrational lines are not exclusive of BGNs, but have been also detected (including vibrational lines of the isotopologues H¹³CN and HC¹⁵N) in galactic hot cores (Rolffs et al. 2011a,b,c) although with significantly lower $L_{\text{HCN } \nu_{23-2}}/L_{\text{IR}}$ ratio in the case of Sgr B2(M) (Aalto et al. 2015b). One interesting point that Rolffs et al. (2011b,c) emphasized is the role of the continuum optical depth in explaining the HCN vibrational emission. Once the dust becomes optically thick to its own radiation, the dust emission is trapped and its diffusion enhances the inner dust temperature (T_{dust}). Dust is heated through absorption of infrared photons coming from the full 4π sr even if the heating source is located at the center, i.e. backwarming (first discussed by Rowan-Robinson 1982) is key to increase T_{dust} . This “greenhouse” effect is very efficient in raising T_{dust} as it works in the continuum, i.e. at all relevant wavelengths—rather than through bands of molecules at specific wavelength ranges, as in the atmosphere of the Earth¹. In addition, the greenhouse effect is evidently taking place in BGNs, as the far-IR molecular line absorption observed with *Herschel*/PACS in these galaxies demonstrates that the continuum behind is

¹ An additional obvious difference is that the heating source in the case of the Earth is external, with photons penetrating the atmosphere owing to its transparency at their wavelengths, while in the present case the heating source is internal; nevertheless, the ultimate reason for the extra heating is in both cases the trapping of radiation in the infrared and implied backwarming.

optically thick in the far-IR (González-Alfonso et al. 2015) and, in some extreme cases, even at millimeter wavelengths (Sakamoto et al. 2013, 2017; Scoville et al. 2017).

In this paper, we develop on the greenhouse effect in BGNs to quantitatively explore to which extent the observed fluxes of the HCN vibrational lines can be understood upon values of physical parameters that are inferred from independent methods; specifically, the column densities, luminosity surface densities, absolute luminosities, and HCN abundances. An oversimplified spherical symmetry is used in the present study that, nevertheless, gives a solid basis on the problem because of the reduced number of involved free parameters. We model the T_{dust} profile in §2 for pure AGN and pure SB models; these T_{dust} profiles are used in §3 to model the HCN vibrational emission and to compare the modeling results with observations. Our main results, including the use of spherical symmetry, are discussed in §4, and the conclusions are summarized in §5. Predictions for HC₃N and HNC vibrational emission will be studied in a future work.

2. MODELS FOR THE CONTINUUM

2.1. Description of the models

The models for the continuum aim to compute the dust temperature (T_{dust}) profile in the source and the emergent spectral energy distribution (SED), assuming spherical symmetry. These models were used but only briefly described in González-Alfonso & Cernicharo (1999), and we describe them in more detail in Appendix A.

We performed two types of models according to the (dominant) nature of the heating source(s): “AGN” models assume a central source of heating, while starburst (“SB”) models simulate a deposition of energy distributed across the source. In both models, it is assumed that the radiation from the heating source(s) is locally absorbed by dust and re-emitted in the infrared. This approach, which is a good approximation because of the high column densities that characterize these obscured regions², imply that the bulk of the dust is heated by mid- and far-infrared radiation, and hence scattering of radiation can be neglected. In AGN models, the central heating source is a blackbody with temperature $T_{\text{cen}} = 1300$ K and a radius R_{cen} that is set to match the required luminosity $L_{\text{IR}}^{\text{AGN}}$.³ In SB models, there is no central source and the heating of shell m (Γ_m) due to stars is assumed to be proportional to both the density of dust and the total dust mass of the shell, $\Gamma_m \propto \rho_m M_m$, normalized to give the required luminosity ($L_{\text{IR}}^{\text{SB}} = \sum_m \Gamma_m$). Evidently, the pure AGN models are

² X-rays will leak out in our models below with column densities $< 10^{24}$ cm⁻², but they represent $\lesssim 10\%$ of the bolometric luminosity (Risaliti & Elvis 2004; Lusso et al. 2012).

³ We use L_{IR} as an equivalent of the bolometric luminosity because the bulk of the luminosity in our models is emitted in the infrared.

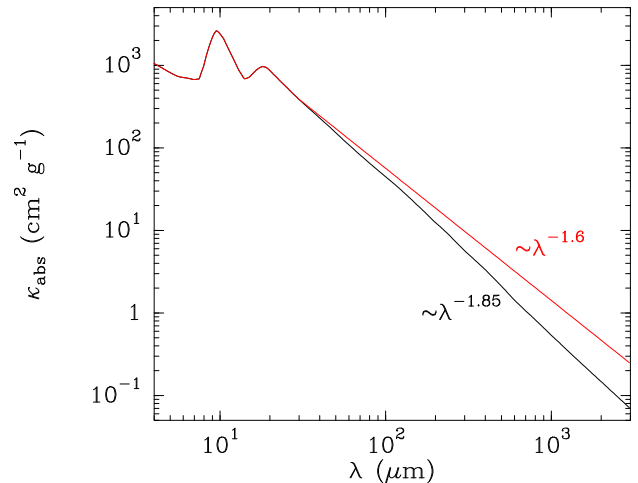


Figure 1. The two curves of mass absorption coefficient of dust as a function of wavelength considered in this work. We use as fiducial the red curve, with an emissivity index of $\beta = 1.6$ and $\kappa_{\text{abs}} = 1.2$ cm² g⁻¹ of dust at $\lambda = 1.1$ mm.

highly idealized in sources with high column densities, where star formation is unavoidable, and represent an extreme limit still useful to potentially address, from comparison with SB models, the possible presence of an extremely buried and energetically dominant AGN. In addition, the SB models obviously smooth out the variation of dust temperatures within any shell as a result of star formation therein, so that the dust temperatures should be considered as mass-averaged within the shell. On the other hand, while both types of models aim to simulate the BGN as a single source, they can also be applied to a collection of independent (not radiatively interacting) sources, provided that the parameters listed below are applicable to each source of the ensemble.

The density profile across the source is described with a power-law $\rho \propto r^{-q}$, with $q = 1, 1.5$. In all our models, a small cavity with radius $R_{\text{int}} = R_{\text{out}}/17$ is adopted, where R_{out} is the outer radius of the source ($R_{\text{int}} > R_{\text{cen}}$ in all AGN models). Figure 1 shows the two curves for the mass absorption coefficient of dust, κ_{abs} , considered in this work. The black curve is the same as used in González-Alfonso et al. (2014), with an emissivity index from the far-IR to millimeter wavelengths of $\beta = 1.85$ and $\kappa_{250 \mu\text{m}} = 8.2$ cm² g⁻¹ of dust at 250 μm . According to Planck Collaboration (2011), however, and for a gas-to-dust ratio of 100, $\kappa_{250 \mu\text{m}}$ is significantly higher, ≈ 14 cm² g⁻¹; in addition, κ_{abs} increases with increasing dust temperature (Mennella et al. 1998). Therefore, we have also used the red curve with the same profile as the black curve at $\lambda < 30$ μm but with $\beta = 1.6$ at longer wavelengths. At 1.1 mm, which is the wavelength of the HCN $\nu_2 = 1^f J = 3-2$ transition, the black and red curves give 0.43 and 1.2 cm² g⁻¹ of dust, which we expect to bracket the actual value. We have used as fiducial the red curve, which gives significant optical

depth at 1.1mm for the maximum column density considered in this work ($N_{\text{H}_2} = 10^{25} \text{ cm}^{-2}$), thus allowing us to study the effect of absorption of dust emission by the HCN vibrational line (§3.2.3). Nevertheless, the T_{dust} profiles obtained with both κ_ν -curves are basically indistinguishable, as T_{dust} depends on the optical depths at $\lambda < 100 \mu\text{m}$. Only results involving the continuum emission at (sub)millimeter wavelengths show differences between the two κ_ν -curves. Our values of κ_{abs} between 7.5 and 50 μm agree within 30% with the values tabulated by Draine (2003).

As shown by Ivezić & Elitzur (1997), the solution of radiative transfer (i.e. the T_{dust} profile and normalized SED) basically depends on dimensionless parameters, but we opt here to use astrophysical parameters applied to the sources of interest: the T_{dust} profile as a function of the normalized radius ($r_n = r/R_{\text{out}}$) depends on the spatial distribution of the heating source(s) (AGN or SB), the luminosity surface density (characterized as $\Sigma_{\text{IR}} = L_{\text{IR}}/(\pi R_{\text{out}}^2)$), the density profile (q), and the H_2 column density N_{H_2} . The latter is determined by assuming a gas-to-dust ratio of 100 by mass; for reference, a radial optical depth at 100 μm of $\tau_{100} = 1$ corresponds to $N_{\text{H}_2} \approx 0.6 \times 10^{24} \text{ cm}^{-2}$.

2.2. Fiducial values

Our models are applied to obscured galaxy nuclei where vibrationally excited HCN has been detected, and the fiducial values listed in Table 1 for N_{H_2} , Σ_{IR} and q can account for most of these observations, as shown below. We use as fiducial N_{H_2} the maximum value considered in this work, 10^{25} cm^{-2} , characteristic of buried sources with bright HCN vibrational emission (e.g. NGC 4418 and Zw 049; Sakamoto et al. 2010, 2013; Costagliola et al. 2013; González-Alfonso et al. 2012; Falstad et al. 2015). More extreme values of $N_{\text{H}_2} \gtrsim 10^{26} \text{ cm}^{-2}$ have been inferred toward the western nucleus of Arp 220 (Scoville et al. 2017; Sakamoto et al. 2017) but, due to the inclination of the disk, these may not be representative of the column averaged over solid angles. We thus conservatively treat the extreme values of $N_{\text{H}_2} > 10^{25} \text{ cm}^{-2}$ by assuming that the T_{dust} profile for $N_{\text{H}_2} = 10^{25} \text{ cm}^{-2}$ is approximately valid (§3.2.3). On the other side, our simulations also cover relatively low values of $N_{\text{H}_2} < 10^{24} \text{ cm}^{-2}$ (Table 1); hence non-BGN sources are also considered. We also adopt as fiducial high values of Σ_{IR} , $(0.55 - 1.1) \times 10^8 L_\odot \text{ pc}^{-2}$, as well as $q = 1$, yielding $L_{\text{IR}}/M_{\text{gas}} = (480 - 960) L_\odot/M_\odot$ for fiducial values. Higher values of $L_{\text{IR}}/M_{\text{gas}}$ may represent sources where negative feedback has cleared the nuclear region from molecular gas.

For a given set of parameters that determine the T_{dust} profile (AGN/SB, Σ_{IR} , q , and N_{H_2}), the absolute flux densities shown below are proportional to the solid angle $\Delta\Omega \equiv \pi R_{\text{out}}^2/D^2$,

where D is the distance to the source⁴. As shown in §3.2.5, $\Delta\Omega$ is in the range $(1 - 3) \times 10^{-2} \text{ arc sec}^2$ for nearby LIRGs with bright HCN vibrational emission, and we adopt as fiducial $\Delta\Omega = 1.1 \times 10^{-2} \text{ arc sec}^2$.

For a given set of values for the parameters in Table 1, D is the only free parameter required to obtain the values of R_{out} , L_{IR} and M_{dust} :

$$R_{\text{out}} = 28.6 \frac{D}{100 \text{ Mpc}} \left(\frac{\Delta\Omega}{1.1 \times 10^{-2} \text{ arc sec}^2} \right)^{1/2} \text{ pc} \quad (1)$$

$$L_{\text{IR}} = 1.4 \times 10^{11} \frac{\Sigma_{\text{IR}}}{5.5 \times 10^7 L_\odot \text{ pc}^{-2}} \left(\frac{D}{100 \text{ Mpc}} \right)^2 \times \frac{\Delta\Omega}{1.1 \times 10^{-2} \text{ arc sec}^2} L_\odot \quad (2)$$

$$M_{\text{dust}} = (1.7 - 2.9) \times 10^6 \frac{N_{\text{H}_2}}{10^{25} \text{ cm}^{-2}} \left(\frac{D}{100 \text{ Mpc}} \right)^2 \times \frac{\Delta\Omega}{1.1 \times 10^{-2} \text{ arc sec}^2} M_\odot, \quad (3)$$

where the two values of M_{dust} correspond to $q = 1.5 - 1.0$, respectively. For fixed fiducial parameters (AGN/SB, Σ_{IR} , N_{H_2} , q , and $R_{\text{out}}/R_{\text{int}}$), absolute luminosities and masses are $\propto R_{\text{out}}^2$.

2.3. Results

Figure 2 compares results for two AGN models (solid lines) and two SB models (dashed lines) that only differ in the column density, $N_{\text{H}_2} = 10^{23} \text{ cm}^{-2}$ (blue curves) and 10^{25} cm^{-2} (red curves, see panel a); all other parameters correspond to the fiducial values. In both models (AGN and SB) with $N_{\text{H}_2} = 10^{25} \text{ cm}^{-2}$, trapping of continuum photons is extremely efficient, thereby strongly increasing T_{dust} in the innermost regions relative to models with the same luminosity but lower N_{H_2} (see Fig. 2c). Nevertheless, the mid-IR continuum in these models can only probe the externalmost shells, and the apparently paradoxical effect of a colder SED but a warmer T_{dust} over the bulk of the source (relative to models with the same luminosity but lower columns, see panels b and c) is obtained for extreme N_{H_2} . This greenhouse effect is also illustrated in panel d, which shows an enhancement of the mean intensity at mid-IR wavelengths within the cocoon of dust by a factor of $\gtrsim 10$. This is the radiation field that pumps the vibrationally excited states of the cyanopolynes, which will then enter in resonance with the greenhouse effect to produce strong vibrational emission.

The radiative diffusion timescale, $t_{\text{diff}} \sim \tau_{\text{dust}} R_{\text{out}}/c$ is evaluated for 25 μm photons and $N_{\text{H}_2} = 10^{25} \text{ cm}^{-2}$ as $t_{\text{diff}} \sim 10^4 (\tau_{\text{dust}}/200) (R_{\text{out}}/20 \text{ pc}) \text{ yr}$. This is much shorter than

⁴ In case of high redshift sources, flux densities scale proportional to $\pi R_{\text{out}}^2(1+z)/D_L^2$, where D_L is the luminosity distance.

Table 1. Model parameters

Parameter	Fiducial value	Explored range	Meaning
AGN-SB		Both	AGN or starburst (SB) generation of the luminosity
$\Sigma_{\text{IR}} (\text{L}_{\odot} \text{pc}^{-2})$	$(5.5 - 11) \times 10^7$	$(1.4 - 22) \times 10^7$	Surface brightness = $L_{\text{IR}}/(\pi R_{\text{out}}^2)$
$N_{\text{H}_2} (\text{cm}^{-2})$	10^{25}	$10^{23} - 10^{25}$	Column density of H_2 along a radial path (from R_{int} to R_{out})
q	1.0	1.0–1.5	Gas and dust density profile ($n \propto r^{-q}$)
$R_{\text{out}}/R_{\text{int}}$	17	–	Outer-to-inner radius of the source
$X_{\text{HCN}}/\Delta V ((\text{km s}^{-1})^{-1})$	1.5×10^{-8}	–	HCN abundance (relative to H_2) per unit velocity interval
$\Delta V (\text{km s}^{-1})$	67	–	Gas velocity dispersion (one-dimensional FWHM)
$\Delta\Omega (\text{arc sec}^2)$	1.1×10^{-2}	–	Solid angle = $\pi R_{\text{out}}^2/D^2$, relevant for absolute values

the dynamical time scale ($> 10^7$ yr) and BGNs will attain radiative equilibrium.

While the predicted SEDs for AGN and SB models are basically indistinguishable for $N_{\text{H}_2} = 10^{25} \text{ cm}^{-2}$ (even at $\lambda < 10 \mu\text{m}$, outside of Fig. 2b), the AGN models have significantly higher T_{dust} in the innermost regions (Fig. 2c). In SB models, the infrared luminosity generated per unit radial interval is $dL_{\text{IR}}/dr \propto r^{2(1-q)}$, which is flat for $q = 1$. An important fraction of the luminosity is thus generated close to the surface with more chance to escape, thus decreasing T_{dust} in the innermost regions relative to AGN models.

The green curve in Fig. 2c indicates the T_{dust} profile in the optically thin limit for parameters other than the column density equal to fiducial values ($\Sigma_{\text{IR}} = 5.5 \times 10^7 \text{ L}_{\odot} \text{pc}^{-2}$, $q = 1$) and the AGN approach. The slope of this curve is $s = -d \log T_{\text{dust}}/d \log r \approx 0.4$, lower than the value of 0.5 expected for grey dust grains (i.e. κ_{abs} independent of λ) due to the decreasing thermal cooling efficiency with decreasing T_{dust} . The AGN model with $N_{\text{H}_2} = 10^{23} \text{ cm}^{-2}$ shows a similar T_{dust} profile, though already showing some effects of trapping, but the $N_{\text{H}_2} = 10^{25} \text{ cm}^{-2}$ AGN model shows a higher slope of $s \approx 0.6$ for $r/R_{\text{out}} < 0.5$ and even higher in the external regions. By contrast, the SB model with $N_{\text{H}_2} = 10^{25} \text{ cm}^{-2}$ shows a slope of only $s \lesssim 0.2$ in the inner $r/R_{\text{out}} < 0.3$ region.

The steep slope s of $T_{\text{dust}}(r)$ in AGN models with high N_{H_2} implies that, for thermal equilibrium between dust and gas, the gas in the inner regions will be unstable under adiabatic radial displacements. The criterion for convective instability translates into the condition $s > q(\gamma - 1)$, where γ is the adiabatic index of the gas. For $T_{\text{dust}} \gtrsim 200 \text{ K}$, the excited rotational levels of H_2 are populated and $\gamma \sim 1.4$, so that the instability criterion $s > 0.4q$ is met in AGN models. For SB models, however, the innermost $r/R_{\text{out}} < 0.3$ regions are stable. In the outermost layers of both AGN and SB models

$s > 1$ and these regions, where the far-IR molecular absorption is produced, will be convective. Convection in BGNs is expected to generate turbulence, and would also modify the temperature (and density) structures of our models, but its quantitative assessment is beyond the scope of this paper.

We show in Fig. 3 the “photosphere” effect that we may expect in nuclei with high $N_{\text{H}_2} = 10^{25} \text{ cm}^{-2}$ (González-Alfonso et al. 2012). With these extreme columns and $q = 1$, the observer can only penetrate $\lesssim 20\%$ of the source radius for $\lambda \lesssim 100 \mu\text{m}$. In this external region, both the AGN and SB models of Fig. 2 ($\Sigma_{\text{IR}} = 5.5 \times 10^7 \text{ L}_{\odot} \text{pc}^{-2}$) yield T_{dust} between 85 and 160 K, in general agreement with the values inferred from far-IR molecular absorption lines in the most buried sources (NGC 4418, Arp 220, Zw 049.057). At (sub)millimeter wavelengths, the penetration is constrained by the optical depth of the observed line.

One important implication of the greenhouse effect is that $\Upsilon_{\text{IR}} \equiv 4\pi r^2 \sigma_{\text{SB}} T_{\text{dust}}(r)^4$ is not conserved through the source, but is much higher than L_{IR} over most volume for high N_{H_2} . This is illustrated in Fig. 4a for the same models as in Fig. 2. The infrared luminosity inferred from T_{dust} and the apparent size may be overestimated by a large factor when selectively probing the innermost regions of the BGN. An alternative way to estimate the source luminosity is integrating the inferred $\sigma_{\text{SB}} T_{\text{dust}}^4$ over the sky plane, using the observed T_{dust} distribution, and multiplying by 2 to account for the two faces of the disk (Wilson et al. 2014; Sakamoto et al. 2017). We have performed a similar calculation in Fig. 4b (Ψ_{IR}) by using the brightness temperature $T_{\text{B}}(1.1 \text{ mm})$, rather than T_{dust} , as a function of the impact parameter p . Results strongly depend on the optical depth at the observed wavelength (1.1 mm in our case). For $N_{\text{H}_2} = 10^{25} \text{ cm}^{-2}$, $\tau_{\text{dust}}(1.1 \text{ mm}) \approx 0.4$ (Fig. 2a) and $\Psi_{\text{IR}}(\text{AGN})$ gives a good estimate to L_{IR} while $\Psi_{\text{IR}}(\text{SB})$ underestimates it by a factor of

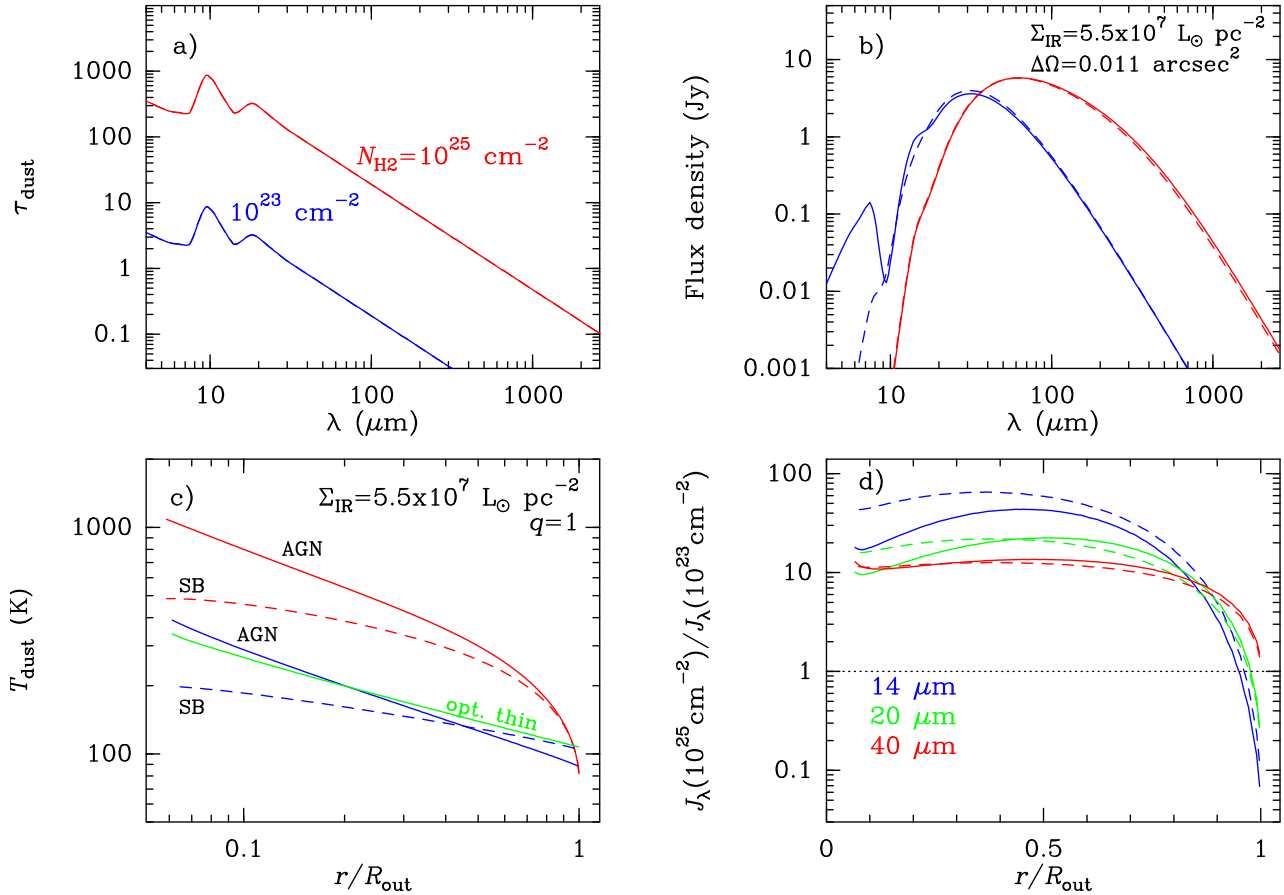


Figure 2. Results of two continuum models for an AGN-dominated source (solid lines) and two models for a starburst-dominated source (dashed lines), illustrating the greenhouse effect. The four models, shown with blue and red lines in panels a-c, have the same luminosity surface density ($\Sigma_{\text{IR}} = 5.5 \times 10^7 L_{\odot} \text{ pc}^{-2}$), solid angle ($\Delta\Omega = 1.1 \times 10^{-2} \text{ arcsec}^2$), and the density varies as r^{-1} ($q = 1$). The models differ only in the column density (panel a): $N_{\text{H}_2} = 10^{25}$ (red) and $N_{\text{H}_2} = 10^{23}$ (blue) cm^{-2} . The predicted SED of the blue (thinner) model is warmer than the red (thicker) model (panel b), because in the former the observer penetrates much inside the cocoon of dust with warmer material. Nevertheless, T_{dust} is on average much higher for the red (thicker) models (panel c), due to trapping of continuum photons. In panel c, the green curve indicates the optically thin limit for the AGN model, with $T_{\text{dust}} \propto r^{-0.4}$ (see text). Within the cocoon of dust, the radiation field at 14, 20, and 40 μm , responsible for the excitation of HCN $\nu_2 = 1$, HC₃N $\nu_6 = 1$, and HC₃N $\nu_7 = 1$ states, is dramatically enhanced for the thick models. The calculated mean intensities $\langle J \rangle$ at the wavelengths of the HCN and HC₃N ro-vibrational lines have large enhancement factors ($\gtrsim 10$, panel d). Therefore, the HCN and HC₃N ro-vibrational lines enter in “resonance” with the greenhouse effect under conditions of high columns, generating strong cyanopolynes emission from the excited vibrational states.

≈ 3 . However, once the continuum at 1.1 mm becomes optically thick, Ψ_{IR} may overestimate L_{IR} by an important factor.

Figure 5 shows the dependence of $\langle T_{\text{dust}} \rangle$, the mass-averaged T_{dust} ($\int \rho(r) T_{\text{dust}}(r) r^2 dr / \int \rho(r) r^2 dr$), on model parameters. In order to describe spatial variation of T_{dust} , the average is performed over 3 radial intervals: the innermost $r < R_{\text{out}}/3$ region (blue symbols), the $r < 2R_{\text{out}}/3$ region (red symbols), and the entire source (black symbols), and is shown as a function of N_{H_2} and for both AGN (filled symbols) and SB (open symbols) models. The different panels show results for $\Sigma_{\text{IR}} = 5.5 \times 10^7$ (upper panels) and $\Sigma_{\text{IR}} = 1.4 \times 10^7 L_{\odot} \text{ pc}^{-2}$ (lower panels), and for $q = 1.0$ and 1.5 (left-hand and right-hand panels, respectively). While there is in all models a contrast between the temperature in the in-

nermost regions and the value averaged over the full source, the strongest contrast corresponds to models with $N_{\text{H}_2} \gtrsim 10^{24} \text{ cm}^{-2}$, giving in AGN models $\langle T_{\text{dust}} \rangle \gtrsim 200\text{--}300 \text{ K}$ for $r < R_{\text{out}}/3$ and $\Sigma_{\text{IR}} = (1.4\text{--}5.5) \times 10^7 L_{\odot} \text{ pc}^{-2}$, respectively. While the AGN models yield similar $\langle T_{\text{dust}} \rangle$ for $q = 1$ and $q = 1.5$, the SB models give significantly higher temperatures for $q = 1.5$, because the radiation is in the latter case more centrally generated.

Appendix A shows the T_{dust} profiles calculated for most performed models, and the results of fitting these profiles to analytic curves that give accurate results for T_{dust} within 10% at all radii.

2.4. Radiation pressure

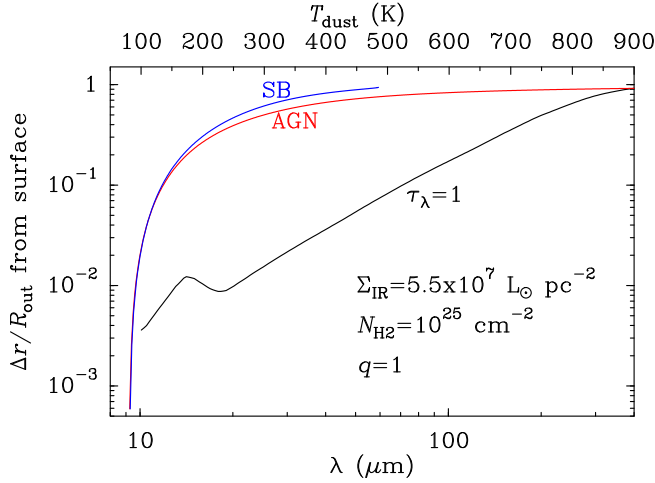


Figure 3. The black line indicates the thickness of the photosphere ($\Delta r/R_{\text{out}}$ from the surface for $\tau_\lambda = 1$, along the sightline that passes through the center of the source) as a function of wavelength (lower horizontal axis) for $N_{\text{H}_2} = 10^{25} \text{ cm}^{-2}$ and $q = 1$. The colored lines show the calculated T_{dust} profile (upper horizontal axis) as a function of $\Delta r/R_{\text{out}}$ for the two models with $N_{\text{H}_2} = 10^{25} \text{ cm}^{-2}$ of Fig. 2 (and fiducial values in Table 1).

We evaluate in Fig. 6 the interplay between radiation pressure and gravity in our modeled sources. As backwarming is key to evaluate T_{dust} in models with high column densities, *backpressure* is equally important to compute the net outward force due to radiation pressure (see Appendix A). In Fig. 6a-b, the radial profiles of the outward, inward, and net (outward–inward) forces per unit gas mass (i.e. the acceleration) due to radiation are shown for the AGN and SB models with $\Sigma_{\text{IR}} = 1.1 \times 10^8 L_\odot \text{ pc}^{-2}$, $N_{\text{H}_2} = 10^{25} \text{ cm}^{-2}$, and $q = 1$.

We have estimated the inward force due to gravity as follows: for SB models, we compute the stellar mass in every shell m as $M_*(m) = L_{\text{IR}}(m)/\epsilon$, where $L_{\text{IR}}(m)$ is the luminosity generated in shell m and ϵ is the light-to-mass ratio of the current stellar population. We first note that there is a threshold value of ϵ , ϵ_{th} , below which the radiation pressure support against gravity is not possible. Using $F_{\text{edd}} = 4\pi G c \Sigma_g \kappa_F f_g^{-1}$ (e.g. Andrews & Thompson 2011), where F_{edd} is the Eddington flux, Σ_g is the gas surface density, κ_F is the Rosseland mean opacity (assumed independent of T_{dust}), and f_g is the gas fraction, combined with $f_g^{-1} = 1 + \epsilon^{-1} \Sigma_g^{-1} F_{\text{edd}}$, we get $F_{\text{edd}} = \epsilon_{\text{th}} \Sigma_g / (1 - \epsilon_{\text{th}}/\epsilon)$ where

$$\epsilon_{\text{th}} = \frac{4\pi G c}{\kappa_F} = 1.3 \times 10^3 \left(\frac{\kappa_F}{10 \text{ cm}^2 \text{ g}^{-1}} \right)^{-1} L_\odot / M_\odot. \quad (4)$$

If $\epsilon < \epsilon_{\text{th}}$, radiation pressure support is unattainable regardless of the gas column density and gas fraction, and the source is intrinsically sub-Eddington. A top-heavy stellar initial mass function, combined with a young age, appear to be strong constraints for global radiation pressure support in

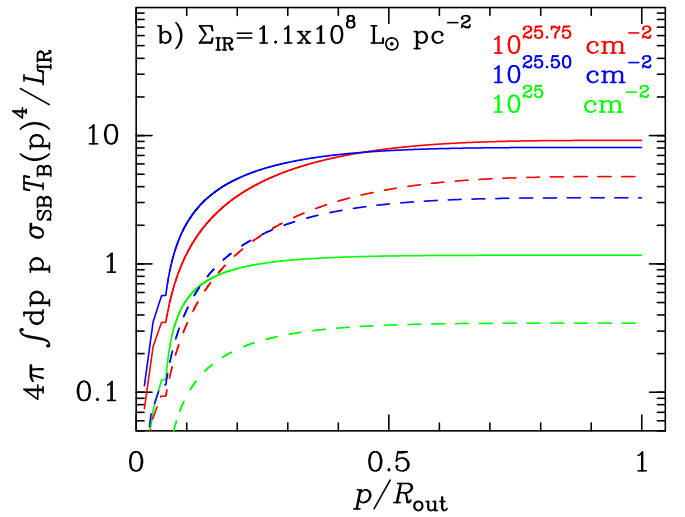
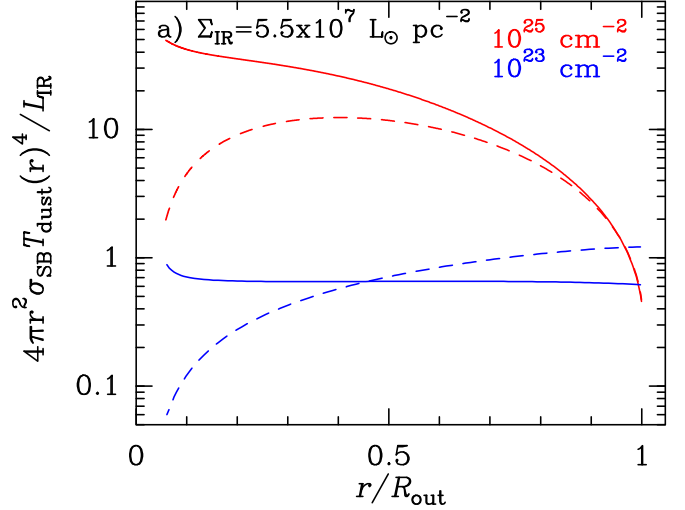


Figure 4. a) The ratio of $\Upsilon_{\text{IR}} \equiv 4\pi r^2 \sigma_{\text{SB}} T_{\text{dust}}(r)^4$ to the luminosity of the source for the same models as in Fig. 2. b) The ratio of $\Psi_{\text{IR}} \equiv 2 \int_0^p dp' 2\pi p' \sigma_{\text{SB}} T_{\text{B}}(p')^4$ to the luminosity of the source, where $T_{\text{B}}(p')$ is the brightness temperature at 1.1 mm for impact parameter p' . Results are shown for $\Sigma_{\text{IR}} = 1.1 \times 10^8 L_\odot \text{ pc}^{-2}$ and three values of N_{H_2} ; solid and dashed lines correspond to AGN and SB models, respectively.

starburst galaxies. Following Förster Schreiber et al. (2003) we choose two values for ϵ that lie above and below ϵ_{th} : a high value of $\epsilon_{\text{H}} = 1700 L_\odot / M_\odot$, which corresponds to the modeled value for a young starburst with a Salpeter (1955) initial mass function and a lower cutoff mass of $1 M_\odot$, and a lower value of $\epsilon_{\text{L}} = 250 L_\odot / M_\odot$, representing a more aged burst. For $N_{\text{H}_2} = 10^{25} \text{ cm}^{-2}$ and $\Sigma_{\text{IR}} = 1.1 \times 10^8 L_\odot \text{ pc}^{-2}$, the gas fractions are $f_{\text{gas}} = 0.63$ and 0.33 for ϵ_{H} and ϵ_{L} , respectively, decreasing for lower values of N_{H_2} .

For AGN models, we simply assume that $M_*(m) = 3 \times M_{\text{gas}}(m)$ in every shell, which can be attributed to an old stellar population. The central mass is assumed to be $M_{\text{central}} =$

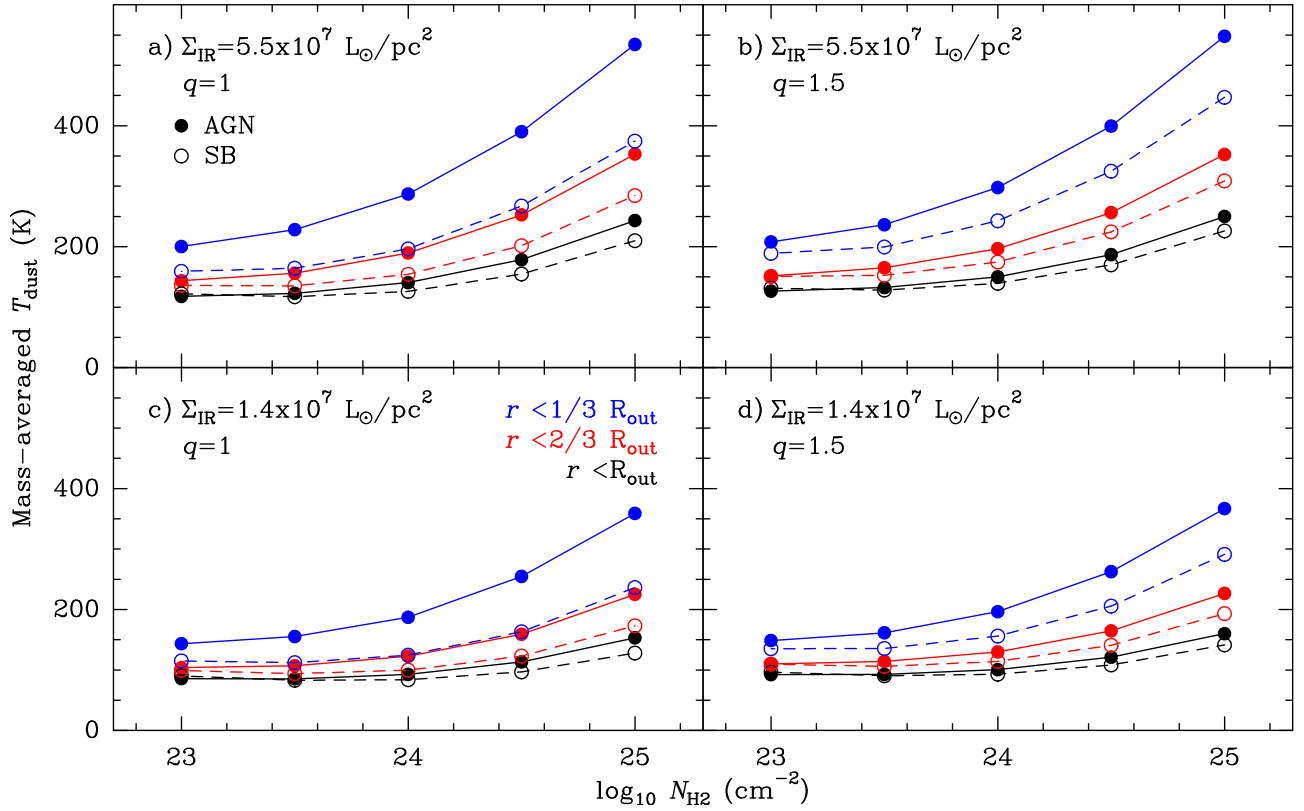


Figure 5. Dependence of the mass-averaged T_{dust} on the surface brightness ($\Sigma_{\text{IR}} = L_{\text{IR}}/\pi R_{\text{out}}^2$), density profile (q), and fractional volume over which the average is performed. Full circles (solid lines) and open circles (dashed lines) indicate AGN and SB models, respectively. As labeled in panel c, blue symbols show $\langle T_{\text{dust}} \rangle$ for the innermost $r < R_{\text{out}}/3$ region, red symbols for the $r < 2R_{\text{out}}/3$ region, and black symbols show $\langle T_{\text{dust}} \rangle$ for the entire source. Upper panels show results for $\Sigma_{\text{IR}} = 5.5 \times 10^7 L_{\odot} \text{pc}^{-2}$, with both (a) $q = 1$ and (b) $q = 1.5$, and lower panels show results for $\Sigma_{\text{IR}} = 1.4 \times 10^7 L_{\odot} \text{pc}^{-2}$.

$2 \times 10^{-4} L_{\text{IR}}$ (in solar units). This is a factor 6 above the Eddington limit ($M_{\text{BH}} = 3 \times 10^{-5} L_{\text{Edd}}$), but M_{central} should include both the black hole mass and the surrounding gas feeding it. The values of the acceleration in Fig. 6a-b are scale invariant.

Figure 6a-b shows that, in the AGN and SB- ϵ_{H} models, the force due to radiation pressure is close to the gravity force in the innermost regions, but gravity overcomes radiation pressure in the external regions where T_{dust} drops. As expected, radiation pressure cannot support the structure in the SB model with ϵ_{L} .

Considering each modeled source as a whole, Fig. 6c-d plots the net force on the whole gas due to radiation pressure, normalized to L_{IR}/c , as a function of N_{H2} and of the corresponding net force due to gravity. Both AGN and SB models with $\Sigma_{\text{IR}} = (5.5 - 22) \times 10^7 L_{\odot} \text{pc}^{-2}$ are plotted. For $N_{\text{H2}} = 10^{25} \text{cm}^{-2}$, the AGN models yield $F_{\text{rad}}/(L_{\text{IR}}/c) \approx 200$, the continuum optical depth at $\approx 25 \mu\text{m}$ (Fig. 2a). Again, all plotted values are scale invariant. In SB models with ϵ_{L} , F_{grav} is much higher than F_{rad} for all columns and Σ_{IR} values. The AGN and SB (ϵ_{H}) models are closer to the Eddington limit. In addition, we find that F_{rad} can overcome grav-

ity for AGN models with moderate $N_{\text{H2}} < 10^{24} \text{cm}^{-2}$, though this becomes hard in sources with very high column densities. Since real systems are expected to be a combination of our pure AGN and SB models with several ages, this result could shed some light on the lack of wide angle outflows in OH, in BGNs with extreme column densities (Falstad et al. 2019), provided that the AGN is not luminous enough to generate a hot bubble that would drive an energy-conserving outflow (e.g. Faucher-Giguère & Quataert 2012; Richings & Faucher-Giguère 2017). We conclude that our models may represent BGNs close to radiation pressure support (Scoville 2003), though feedback through a hot bubble or winds is probably required to launch a wide-angle outflow in real systems with typical column densities of a few $\times 10^{23} \text{cm}^{-2}$ (González-Alfonso et al. 2017).

3. MODELS FOR HCN

3.1. Description of the models

The models for HCN include 25 rotational levels -ignoring hyperfine structure- in the ground vibrational state ($v = 0$) and, because of the l -doubling in the $\nu_2 = 1$ bending state, up to 48 levels in $\nu_2 = 1$, with a maximum energy above the

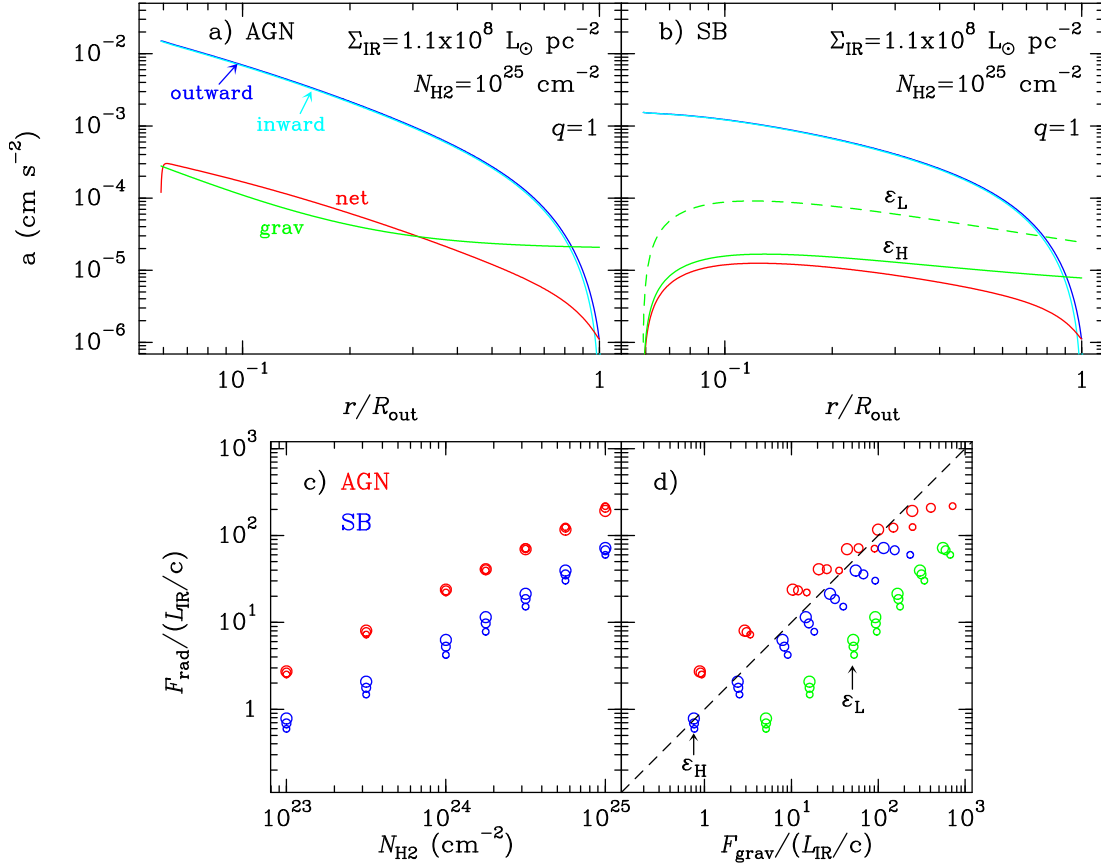


Figure 6. *Upper:* Radial profiles of the acceleration (force per unit gas mass) due to radiation pressure on dust, for (a) AGN and (b) SB models, with parameters specified. The dark and light blue curves show the outward and inward accelerations, respectively, and the net (outward) acceleration is shown in red. The green curves show the inward acceleration due to gravity that, for the SB model, has been calculated for two values of ϵ , the light-to-mass ratio of the stellar population (denoted as ϵ_{H} and ϵ_{L} , see text). *Lower:* The net force due to radiation pressure is plotted as a function of (c) N_{H_2} and (d) the net force due to gravity, for both AGN (red) and SB (blue and green) models. Small, medium, and large circles indicate $\Sigma_{\text{IR}} = 5.5 \times 10^7$, 1.1×10^8 , and $2.2 \times 10^8 L_{\odot} \text{ pc}^{-2}$. All values are scale invariant.

ground level of 2300 K ($\nu_2 = 1$, $J = 24$) and giving a total of 165 transitions (including the direct l -type transitions within $\nu_2 = 1$ at centimeter wavelengths). The models use the T_{dust} profiles obtained in the previous section, and assume thermal equilibrium between dust and gas ($T_{\text{gas}} = T_{\text{dust}}$). For HCN, however, there is no need of the large number of shells required for T_{dust} calculations (Appendix A), so that the T_{dust} profiles were smoothed and 30 shells were used for molecular calculations. The approach described in González-Alfonso & Cernicharo (1997, 1999) was used to calculate the equilibrium populations and emergent spectra, and the molecular excitation by dust-emitted photons was treated assuming that gas and dust are mixed. Absorption of line emitted photons by dust (extinction) is taken into account for all transitions. Calculations for HCN include overlaps between the Q-branch ro-vibrational lines, as well as between the blended $\nu = 0$ and $\nu_2 = 1^e$ rotational lines. For simplicity, no velocity gradients are included.

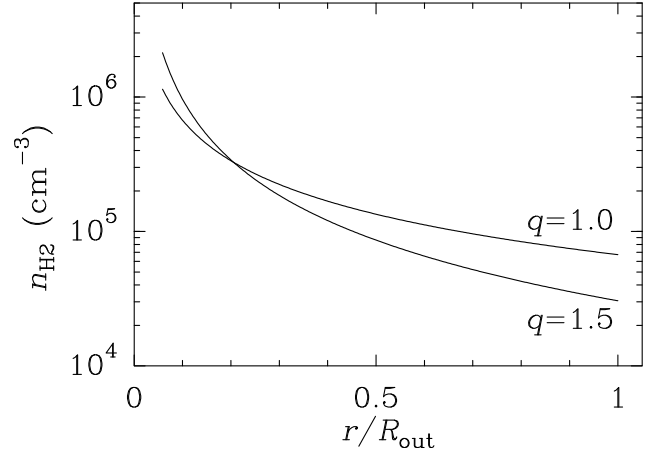


Figure 7. The density profile for $N_{\text{H}_2} = 10^{25} \text{ cm}^{-2}$, $R_{\text{out}} = 17 \text{ pc}$, and $q = 1.0 - 1.5$. In spherical symmetry, densities scale as $\propto N_{\text{H}_2} R_{\text{out}}^{-1}$, but we neglect the R_{out}^{-1} dependence to account for more general geometries (see text).

Collisional excitation from the ground to the $\nu_2 = 1$ vibrational state is ignored, as well as among levels within the $\nu_2 = 1$ state. Collisional rates among rotational levels of the ground $\nu = 0$ state are taken from [Dumouchel et al. \(2010\)](#). Unlike the continuum models developed in §2, line excitation models have the source size (R_{out}) as an independent parameter in addition to N_{H_2} and others in Table 1. This is because collisional excitation depends on the local gas density n_{H_2} , which in spherical symmetry is proportional to $N_{\text{H}_2} R_{\text{out}}^{-1}$. Despite this dependence on R_{out} , we use a simplified approach in our modeling to adopt the n_{H_2} profiles (as a function of r/R_{out}) in Fig. 7 for any R_{out} , and scale n_{H_2} with N_{H_2} . The density profiles in Fig. 7 are exact for $R_{\text{out}} = 17$ pc. This simplification shrinks the model-parameter space and is partly justified by noting that N_{H_2} , n_{H_2} , and R_{out} do not necessarily have a direct link in realistic situations where the gas distribution is neither smooth nor spherically symmetric: in a flat structure like an inclined disk, the solid angle subtended by the source yields a scale length in the plane of sky $R_{\text{out}} = D\sqrt{\Delta\Omega/\pi}$, but the scale length along the line of sight $N_{\text{H}_2}/n_{\text{H}_2}$ is an independent parameter. We thus unlink the values of n_{H_2} from R_{out} to approximately account for more general geometries, and discuss below the impact of the adopted density profiles on results.

Assuming that the HCN abundance relative to H_2 , X_{HCN} , is uniform across the source, the excitation of HCN for a given continuum model and density profile depends on $N_{\text{HCN}}/\Delta V$, the HCN column density (along a radial path) per unit of velocity interval. Line broadening is simulated with a microturbulent approach. For given $N_{\text{HCN}}/\Delta V$, the emergent line fluxes are proportional to the velocity dispersion ΔV . In NGC 4418, pure rotational HCN lines have been detected in absorption with *Herschel*/PACS at far-IR wavelengths (135–190 μm , up to at least $J = 25 - 24$), suggesting high column densities of HCN ([González-Alfonso et al. 2012](#)). For $\text{HCN}/\text{H}_2\text{O} = 0.1 - 0.3$ and $\text{H}_2\text{O}/\text{H} \sim 10^{-5}$, we expect $X_{\text{HCN}} \sim 10^{-6}$ in these nuclear regions, which we adopt as fiducial value. A similar HCN abundance was derived by [Lahuis et al. \(2007\)](#) in BGNs from the analysis of the 14 μm band, and chemical calculations also favor high X_{HCN} in very warm regions ([Harada et al. 2010](#)). On the other hand, ΔV should approximately characterize the velocity dispersion measured in the nuclear regions of (U)LIRGs after correcting for the rotation velocity; i.e. ΔV is the velocity dispersion along a typical line of sight through the nucleus. In the nuclear regions of ULIRGs, ΔV is high ($\gtrsim 100 \text{ km s}^{-1}$) as measured from the CO lines (e.g. [Downes & Solomon 1998](#)), but CO probably probes more extended gas than that associated with the HCN vibrational emission. In the LIRG IC 860, where the HCN $\nu_2 = 1^f J = 3 - 2$ line is unblended from the neighboring $\text{HCO}^+ 3 - 2$ line, the HCN vibrational line has $\text{FWHM} = 130 \text{ km s}^{-1}$ ([Aalto et al. 2015b](#)),

with some broadening attributed to the rotation. We adopt a fiducial $\Delta V = 67 \text{ km s}^{-1}$ with the simplified assumption that ΔV is uniform and hence independent of the impact parameter p , and then $N_{\text{HCN}}/\Delta V = 1.5 \times 10^{17} \text{ cm}^{-2}/(\text{km s}^{-1})$ for $N_{\text{H}_2} = 10^{25} \text{ cm}^{-2}$. Since N_{HCN} is uniquely determined by N_{H_2} and X_{HCN} , we list in Table 1 the fiducial values for $X_{\text{HCN}}/\Delta V$ and ΔV .

As it is the case for the continuum, line fluxes are proportional to $\Delta\Omega = \pi R_{\text{out}}^2/D^2$ for fixed values of the fiducial parameters in Table 1.

3.2. Results

3.2.1. HCN excitation and line optical depths

The excitation of HCN is illustrated in Fig. 8a-f through the comparison between the T_{dust} profiles and the excitation temperatures (T_{EX}) of the HCN Q(3), $\nu = 0 J = 3 - 2$, and $\nu_2 = 1^f J = 3 - 2$ lines. As shown in the upper panels (a, c, and e), the excitation is extremely simple for $N_{\text{H}_2} = 10^{25} \text{ cm}^{-2}$, as the three lines are in LTE at $T_{\text{gas}} = T_{\text{dust}}$ even for moderate $\Sigma_{\text{IR}} = 1.4 \times 10^7 \text{ L}_\odot \text{ pc}^{-2}$. Collisional excitation is able to thermalize the HCN $\nu = 0$ low- J levels at T_{gas} , and the Q(3) line, connecting the $\nu = 0 J = 3$ and $\nu_2 = 1^f J = 3$ levels, is also thermalized at the local T_{dust} . As a consequence, the $\nu_2 = 1^f J = 3 - 2$ line is also thermalized.

The HCN ground-state levels can be excited either via collisional events and/or by radiative pumping to the ν_2 state and subsequent decay. If the column density is decreased by a factor 10 (Fig. 8b-d-f, with $N_{\text{H}_2} = 10^{24} \text{ cm}^{-2}$), n_{H_2} drops by the same factor (Fig. 7) and collisions are unable to thermalize the $\nu = 0$ low- J lines in the external regions (Fig. 8d). The departure from LTE occurs at $T_{\text{dust}} \lesssim 200 \text{ K}$, because radiative excitation is still able to thermalize the $\nu = 0$ low- J levels at higher T_{dust} . Nevertheless, the Q(3) line is still in LTE at all radii (Fig. 8b) because the continuum at 14 μm remains very optically thick (Fig. 2a). Therefore, the excitation of the $\nu_2 = 1^f J = 3 - 2$ line mimics that of the ground $\nu = 0 J = 3 - 2$ line, hence showing the same departure from LTE (Fig. 8d-f).

The maximum optical depths through the source (τ_{max}) of the quoted lines are also shown in Fig. 8g. The HCN $\nu = 0 J = 3 - 2$ line is very optically thick in all models, and as a surface tracer it is unuseful to probe the inner regions of BGNs where radiative excitation is important. The Q(3) line is also saturated. For fixed N_{H_2} , these transitions show higher τ_{max} in models with lower overall excitation, because the population is accumulated in the low- J levels. By contrast, the HCN $\nu_2 = 1^f J = 3 - 2$ line obviously shows higher τ_{max} in higher excitation models, and the mere detection of the line provides evidence for environments with extreme physical conditions. For our fiducial $X_{\text{HCN}}/\Delta V$, this line becomes optically thick for $N_{\text{H}_2} > 10^{24} \text{ cm}^{-2}$ and $\Sigma_{\text{IR}} \gtrsim 5 \times 10^7 \text{ L}_\odot \text{ pc}^{-2}$.

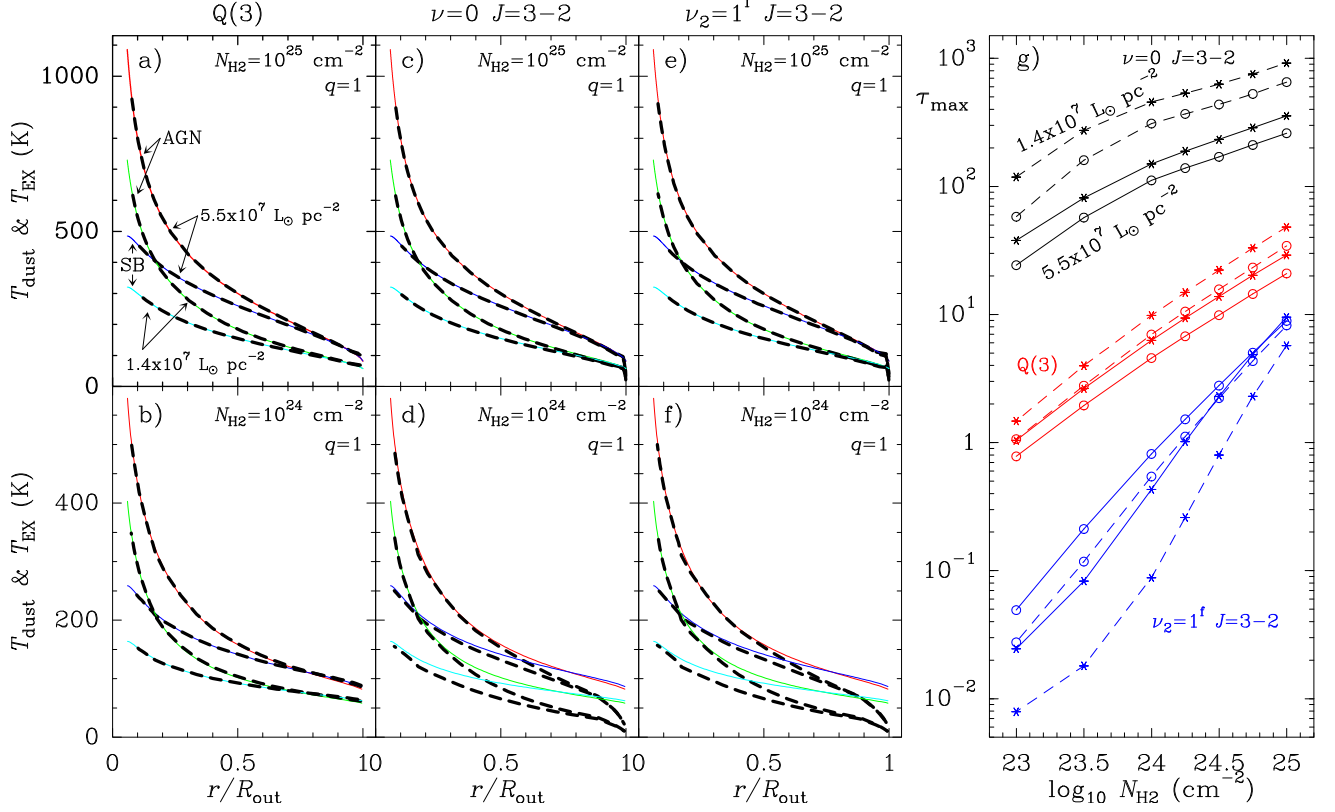


Figure 8. a-f) Comparison between the T_{dust} profiles (colored curves) and the excitation temperature of the HCN Q(3) (a-b), $\nu = 0 J = 3 - 2$ (c-d), and $\nu_2 = 1^f J = 3 - 2$ (e-f) lines (overplotted dashed black curves). In our models we assume $T_{\text{gas}} = T_{\text{dust}}$. As indicated in panel a, the red-green curves indicate AGN models with $\Sigma_{\text{IR}} = (5.5 - 1.4) \times 10^7 L_{\odot} \text{ pc}^{-2}$, while the light-blue and blue curves show the analogous SB models. Upper panels show results for $N_{\text{H}_2} = 10^{25} \text{ cm}^{-2}$, and lower panels for $N_{\text{H}_2} = 10^{24} \text{ cm}^{-2}$; other parameters have fiducial values. g) The maximum line optical depth (at line center and along the sightline that crosses the source tangent to the inner cavity) of the same lines as before ($\nu = 0 J = 3 - 2$ in black, Q(3) in red, and $\nu_2 = 1^f J = 3 - 2$ in blue) as a function of N_{H_2} . Solid and dashed lines correspond to $\Sigma_{\text{IR}} = 5.5 \times 10^7$ and $1.4 \times 10^7 L_{\odot} \text{ pc}^{-2}$, respectively, and circles and starred symbols indicate AGN and SB models, respectively.

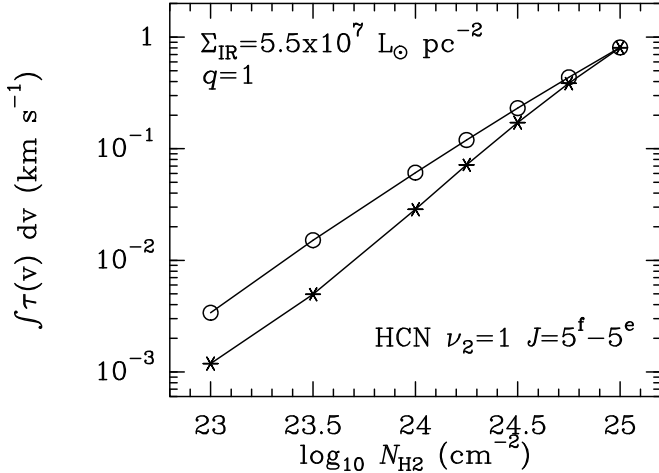


Figure 9. The velocity-integrated line optical depth along a radial path of the direct l -type HCN $\nu_2 = 1 J = 5$ line at 6.73 GHz, for AGN (circles) and SB (stars) models with $\Sigma_{\text{IR}} = 5.5 \times 10^7 L_{\odot} \text{ pc}^{-2}$ and $q = 1$.

We have also checked the excitation and optical depth of the direct l -type transitions ($\Delta J = 0$) in the $\nu_2 = 1$ state at centimeter wavelengths. Three of these lines ($J = 4, 5, 6$) were detected in absorption towards Arp 220 with the Arecibo telescope (Salter et al. 2008). In our models, however, these lines are slightly inverted, although with weak amplification ($|\tau| < 0.3$ for the highest $N_{\text{H}_2} = 10^{25} \text{ cm}^{-2}$). The inversion is due to overlap effects among the ro-vibrational lines that pump the $\nu_2 = 1$ state, and involves a tiny perturbation in the relative populations of the e and f levels because of the low splitting due to l -type doubling (see discussion by Thorwirth et al. 2003). Since collisional coupling among the involved levels, which is not included in our models, is expected to quench the maser in high density regions, we have estimated the velocity-integrated optical depth of the $J = 5$ line at 6.73 GHz by assuming that the sum of the upper and lower level populations remains unchanged, and that the levels are thermalized at the local T_{gas} . Results for $\int \tau(\nu) d\nu$ along a radial path, as a function of N_{H_2} for $\Sigma_{\text{IR}} = 5.5 \times 10^7 L_{\odot} \text{ pc}^{-2}$ and $q = 1$, are shown in

Fig. 9. For $N_{\text{H}_2} = 10^{25} \text{ cm}^{-2}$, $\int \tau(\nu) d\nu \sim 0.8 \text{ km s}^{-1}$ with very similar values for the AGN and SB models. Most of the absorption is produced in the inner layers ($r/R_{\text{out}} \lesssim 0.3$) where $T_{\text{dust}} \gtrsim 300 \text{ K}$. In Arp 220, the value measured by Salter et al. (2008) for this line is $\approx 5 \text{ km s}^{-1}$, which independently indicates the enormous columns of warm HCN gas in the nuclear region of this galaxy.

3.2.2. The impact of the greenhouse effect on the HCN vibrational emission in buried galactic nuclei

Figure 10 illustrates the impact of the greenhouse effect on the HCN $\nu_2 = 1^f J = 3-2$ and $J = 4-3$ emission, by comparing in detail results of the same models as in Fig. 8a,c,e (with $N_{\text{H}_2} = 10^{25} \text{ cm}^{-2}$ and $\Sigma_{\text{IR}} = (1.4-5.5) \times 10^7 L_{\odot} \text{ pc}^{-2}$). As shown in Fig. 10d-e, the HCN $\nu_2 = 1^f J = 3-2$ and $J = 4-3$ lines are optically thick along lines of sight that cross regions with $T_{\text{dust}} \gtrsim 200 \text{ K}$. These are the regions that mostly contribute to the line fluxes, so that the fluxes are nearly proportional to the solid angle subtended by the region with temperatures above $\sim 200 \text{ K}$. For $\Sigma_{\text{IR}} = 5.5 \times 10^7 L_{\odot} \text{ pc}^{-2}$, this region is about twice the size of the model with $1.4 \times 10^7 L_{\odot} \text{ pc}^{-2}$, and hence the modeled fluxes are a factor ~ 4 higher.

As discussed above (Fig. 8a,c,e), the low- J $\nu = 0$, $\nu_2 = 1-0$, and $\nu_2 = 1$ lines are in LTE at the local $T_{\text{gas}} = T_{\text{dust}}$ for the high $N_{\text{H}_2} = 10^{25} \text{ cm}^{-2}$ value considered in Fig. 10, and hence the excitation of the $\nu_2 = 1$ rotational lines is higher in AGN than in SB models. However, the higher excitation of AGN models mainly affect the high- J levels of the $\nu_2 = 1$ state, while the relatively low-lying HCN $\nu_2 = 1^f J = 3, 4$ levels only show a moderate increase of populations ($\lesssim 50\%$ for $\Sigma_{\text{IR}} \gtrsim 5.5 \times 10^7 L_{\odot} \text{ pc}^{-2}$) relative to SB models⁵. In addition, and owing to the quoted line opacity effects in the $\nu_2 = 1$ lines, the innermost regions of the AGN model where T_{dust} is very high are not probed, so that the AGN and SB models with the same Σ_{IR} yield similar line fluxes. The differences in HCN $\nu_2 = 1$ fluxes between AGN and SB models are mostly due to the different spatial scales over which the lines are optically thick, and are larger for moderate Σ_{IR} (Fig. 10d-e). One way to observationally check that the $\nu_2 = 1$ lines saturate is observing both the 3-2 and 4-3 lines. In the optically thick regime, the flux ratio 4-3/3-2 (both in Jy km s^{-1}) is $(\nu_{4-3}/\nu_{3-2})^2 \approx 1.8$. A ratio slightly higher (1.9-2) may also be expected because the 4-3 line is optically thick over a slightly larger spatial extent (this effect is again more pronounced for moderate Σ_{IR} , Fig. 10). However, the opposite effect is obtained ($\nu_2 = 1^f 4-3/3-2 < 1.8$)

⁵ The high T_{dust} regions of AGN models efficiently populate the $\nu = 0$ high- J levels at the expense of the low- J levels, so that the $\nu = 0 J = 2-5$ levels (which pump the $\nu_2 = 1 J = 3-4$) are less populated in AGN than in SB models (with otherwise the same parameters). This effect partially compensates for the higher vibrational excitation of AGN models.

if the (sub)millimeter continuum is bright, because the absorption of the continuum by the lines is stronger for the $\nu_2 = 1^f J = 4-3$ line (§3.2.4); this effect dominates over the different emitting areas in the AGN models, and in the SB model with high Σ_{IR} , of Fig. 10.

For models with $N_{\text{H}_2} = 10^{25} \text{ cm}^{-2}$, and since the $\nu_2 = 1$ lines become optically thick at $T_{\text{EX}} \approx T_{\text{dust}} \gtrsim 200 \text{ K}$, line fluxes can be estimated as

$$F_{\text{HCN } \nu_2} (\text{Jy km s}^{-1}) \sim 10^{23} \frac{2k}{\lambda^2} T_{\text{EX}} \Delta\Omega_{\tau=1} \Delta V, \quad (5)$$

where k is the Boltzmann constant and $\Delta\Omega_{\tau=1}$ is the solid angle subtended by the region where the line saturates (i.e. where $T_{\text{dust}} \approx 200 \text{ K}$). For the $\nu_2 = 1^f J = 3-2$ line, taking $\Delta\Omega_{\tau=1} = 0.6^2 \Delta\Omega$ for the SB model with $\Sigma_{\text{IR}} = 5.5 \times 10^7 L_{\odot} \text{ pc}^{-2}$ (Fig. 10; $\Delta\Omega$ in Table 1) and $\Delta V \sim 100 \text{ km s}^{-1}$ (higher than 67 km s^{-1} due to broadening by line opacity effects), eq. (5) gives 4.1 Jy km s^{-1} , similar to the actual value. Using $\Delta\Omega_{\tau=1} = 0.3^2 \Delta\Omega$ for the $\Sigma_{\text{IR}} = 1.4 \times 10^7 L_{\odot} \text{ pc}^{-2}$ model, eq. (5) yields 1 Jy km s^{-1} , also in rough agreement with the modeled value. Equation (5), and specifically the value of $T_{\text{EX}} = 200 \text{ K}$ for the photosphere of the HCN vibrational emission, can be observationally checked if the rovibrational line is spatially resolved and $\Delta\Omega_{\tau=1}$ is estimated, but we remark that it is only valid for $N_{\text{HCN}} = 10^{19} \text{ cm}^{-2}$.

A few models for H^{13}CN , assuming an abundance ratio relative to HCN of 1/60, have also been computed with fiducial parameters ($\Sigma_{\text{IR}} = 1.1 \times 10^8 L_{\odot} \text{ pc}^{-2}$). The fluxes predicted for the $\text{H}^{13}\text{CN } \nu_2 = 1^f J = 3-2$ and $J = 4-3$ lines are factors 20-25 and 15-18 weaker than the HCN fluxes of the same lines, respectively. Despite the above $\text{H}^{13}\text{CN } \nu_2 = 1^f$ lines are optically thin, the AGN and SB models yield similar fluxes for them because the higher T_{dust} of the AGN models mainly affect the high- J levels of the $\nu_2 = 1$ state and the increase of the $\nu_2 = 1^f J = 3-4$ level populations is moderate.

3.2.3. Spatial profiles

Since the continuum at millimeter wavelengths is less optically thick than the HCN $\nu_2 = 1^f J = 3-2$ line (Fig. 10d-e), and due to the greenhouse effect that is responsible for the high T_{dust} in the innermost regions, the millimeter-wave continuum and HCN vibrational emission are expected to show quite different spatial profiles (Fig. 11). The continuum strongly peaks toward the center, with a profile steeper than the $N_{\text{H}_2}(p)$ profile of our spherically symmetric models (indicated with the green curve in Fig. 11a; $N_{\text{H}_2}(p)$ attains 10^{25} cm^{-2} at $p/R_{\text{out}} \approx 0.45$). By contrast, the brightness of the continuum at $60 \mu\text{m}$, for which a well defined photosphere exists (Fig. 3), is nearly flat (grey curve in Fig. 11a). The bulk of the source luminosity is emitted in the far-IR (Fig. 2b), so that the continuum at millimeter wavelengths, while nicely probing the warm inner regions, may underestimate the area over which the luminosity is re-emitted. On

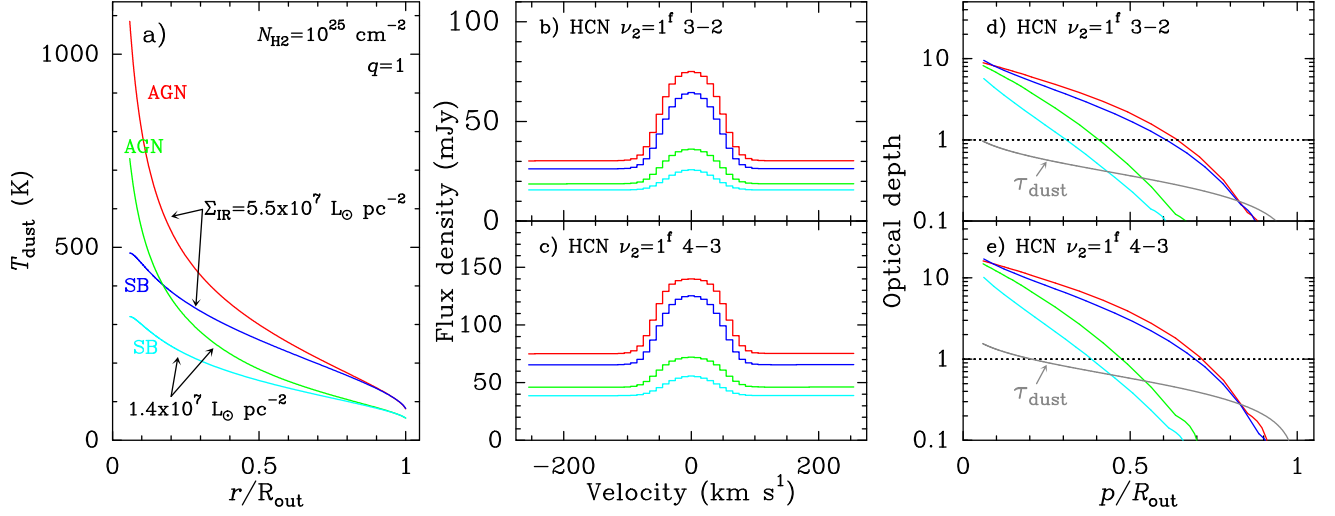


Figure 10. Detailed results for the same models as in Fig. 8a-c-e. a) The T_{dust} profiles. (b-c) The line profiles and (d-e) optical depths at line center of the HCN $\nu_2 = 1^f J = 3-2$ and $4-3$ transitions, with fiducial parameters ($N_{\text{HCN}}/\Delta V = 1.5 \times 10^{17} \text{ cm}^{-2}/(\text{km s}^{-1})$ and $\Delta V = 67 \text{ km s}^{-1}$). In panels d-e, the grey curves indicate the optical depth of the continuum at the wavelengths of the lines (1.1 and 0.84 mm). In panels b-c, a solid angle of $\Delta\Omega = 1.1 \times 10^{-2} \text{ arc sec}^2$ is adopted for the flux density scale. After subtracting the continuum, the HCN $\nu_2 = 1^f J = 3-2$ line fluxes are 4.6 (red), 3.7 (blue), 1.7 (green), and 0.87 Jy km s^{-1} (light blue), while the $\nu_2 = 1^f J = 4-3$ line fluxes are 7.4 (red), 6.3 (blue), 2.7 (green), and 1.6 Jy km s^{-1} (light blue).

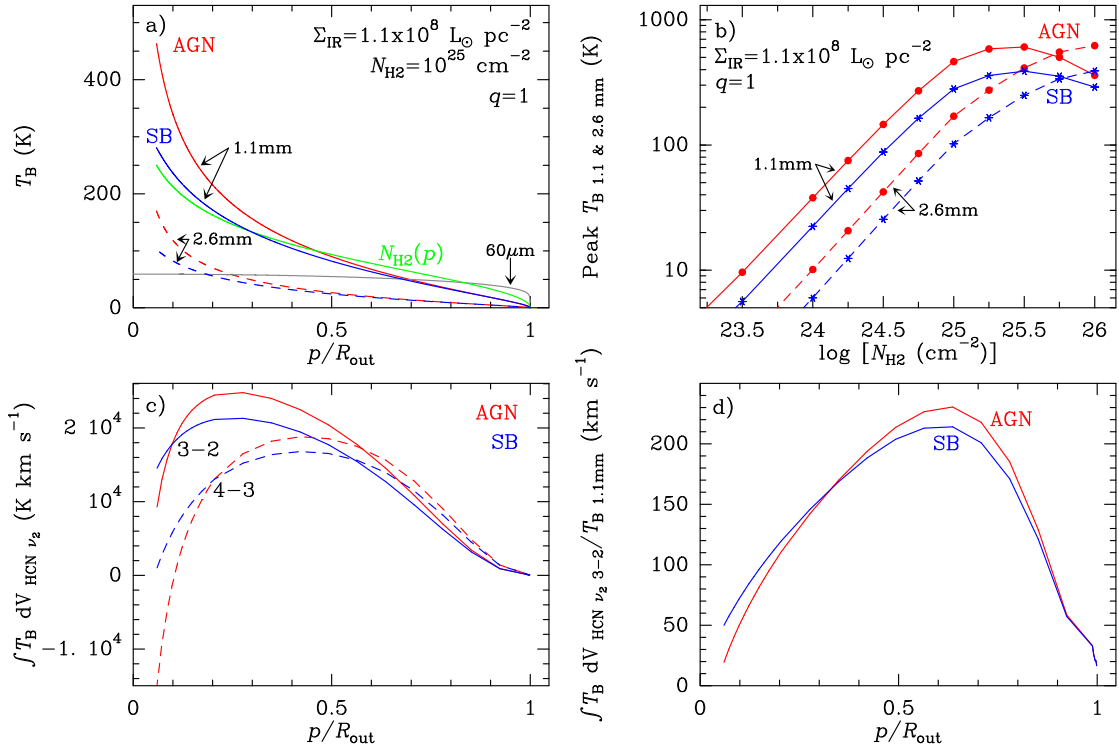


Figure 11. a) The brightness T_B of the continuum at 1.1 mm (solid colored curves) and 2.6 mm (dashed) as a function of the impact parameter, for the fiducial models (AGN in red and SB in blue) with $\Sigma_{\text{IR}} = 1.1 \times 10^8 \text{ L}_\odot \text{ pc}^{-2}$. For comparison, the green curve indicates the $N_{\text{H}_2}(p)$ profile (arbitrarily scaled), and the grey curve shows the T_B profile at $60 \mu\text{m}$ (basically the same for AGN and SB). b) The peak brightness temperature at 1.1 and 2.6 mm as a function of the H_2 column density, for $\Sigma_{\text{IR}} = 1.1 \times 10^8 \text{ L}_\odot \text{ pc}^{-2}$ and $q = 1$. c) The brightness of the velocity-integrated (above the continuum) HCN $\nu_2 = 1^f J = 3-2$ (solid) and $J = 4-3$ (dashed) lines as a function of the impact parameter, for the same models as in panel a. d) The spatial profile of the HCN $\nu_2 = 1^f J = 3-2$ line flux-to-continuum ratio.

the other hand, the velocity-integrated line brightness above the continuum of the HCN $\nu_2 = 1^f J = 3-2$ and $J = 4-3$ lines show a drop of emission toward the center (Fig. 11c) because the line is formed in front of the bright continuum, thus absorbing it⁶. The continuum brightness at 1.1 mm behind the HCN $\nu_2 = 1^f J = 3-2$ photosphere is still insufficient to produce an absorption line (i.e. negative $\int T_B dv$) toward the center, but the $4-3$ line shows a net absorption in the AGN model owing to the increasing optical depth of the continuum and the line. For sufficiently high N_{H_2} , we thus expect a ring-like emission for both the HCN $\nu_2 = 1^f J = 3-2$ and $J = 4-3$ lines, as recently observed in IC 860 (Aalto et al. 2019), and a strongly varying HCN-to-continuum brightness ratio (Fig. 11d). Note that significant absorption of the continuum by the HCN $\nu_2 = 1^f J = 3-2$ line is expected when the HCN line flux-to-continuum ratio, with units of velocity (Fig. 11d), becomes comparable to or lower than the linewidth of the HCN vibrational line, meaning that the total (velocity-integrated) continuum absorbed by the line is comparable to the line flux. Absorption of thermal dust continuum by molecular lines at (sub)millimeter wavelengths has been inferred in several galactic nuclei (e.g. Sakamoto et al. 2009; Martín et al. 2016; Aladro et al. 2018).

Our models with $N_{\text{H}_2} = 10^{25} \text{ cm}^{-2}$ still have too low continuum optical depth at 2.6 mm ($\tau_{2.6\text{mm}} \approx 0.1$ along a radial path, Fig. 2a) to account for the high brightness observed at this wavelength toward Arp 220W (after subtracting the plasma (free-free and synchrotron) emission; Scoville et al. 2017; Sakamoto et al. 2017). To estimate the peak values of T_B due to thermal dust emission in the millimeter at higher column densities, we have simply assumed that the T_{dust} profile remains the same as for $N_{\text{H}_2} = 10^{25} \text{ cm}^{-2}$. Since T_{dust} increases as N_{H_2} increases due to enhanced trapping of radiation, the inferred values of T_B , shown in Fig. 11b, can be considered lower limits for $N_{\text{H}_2} > 10^{25} \text{ cm}^{-2}$. Even so, the 2.6 mm continuum is expected to attain brightnesses of ~ 600 (AGN) and ~ 400 K (SB), the former similar to the strong maximum at 3 mm inferred in Arp 220W from high angular resolution observations (Sakamoto et al. 2017).

Figure 11 is based on the red κ_ν -curve of Fig. 1 that, with a value of $1.2 \text{ cm}^2 \text{ g}^{-1}$ of dust at 1.1 mm, gives $\tau_{1.1\text{mm}} \approx 0.4$ for $N_{\text{H}_2} = 10^{25} \text{ cm}^{-2}$ (Fig. 2). If, however, the black κ_ν -curve is used, the brightness of the 1.1 mm continuum toward the center would be significantly lower and the HCN $\nu_2 = 1^f J = 3-2$ emission would also peak toward the center. In this case, $N_{\text{H}_2} \gtrsim 10^{25.5} \text{ cm}^{-2}$ would be required to obtain the drop of HCN vibrational emission towards the peak of continuum

⁶ Due to absorption of the continuum by the line, there is little continuum emission at line center, so that the apparent drop of line emission is due to the subtraction of the continuum adjacent to the line (i.e. free from line absorption).

emission. In addition, high brightnesses of the 2.6 mm continuum would only be obtained for $N_{\text{H}_2} \sim 10^{26.5} \text{ cm}^{-2}$.

3.2.4. Overall modeling results

Overall results for the HCN $\nu_2 = 1$ fluxes in both AGN and SB models, as a function of N_{H_2} and for all explored values of Σ_{IR} , are displayed in Fig. 12. Other parameters take fiducial values (e.g., $q = 1$, Table 1). Since line fluxes are proportional to the solid angle $\Delta\Omega$ of the source if all other parameters in Table 1 are fixed, the average brightness $F_{\text{HCN}\nu_{23-2}}/\Delta\Omega$ in panel a does not depend on $\Delta\Omega$. Its dependence on other parameters (N_{H_2} , Σ_{IR} , and the choice of AGN/SB) is plotted in Fig. 12a, such that the modeled values can be compared with observations to constrain these parameters. For our fiducial value $X_{\text{HCN}}/\Delta V = 1.5 \times 10^{-8} (\text{km s}^{-1})^{-1}$, $F_{\text{HCN}\nu_{23-2}}/\Delta\Omega$ is also proportional to ΔV and the modeled curves in Fig. 12a would have to be vertically shifted by a factor $\Delta V/(67 \text{ km s}^{-1})$, where ΔV is the actual intrinsic velocity dispersion (i.e. corrected for systemic motions as rotation and for broadening by optically thick effects) of the considered source. For the purposes of this paper, we assume that $\Delta V = 67 \text{ km s}^{-1}$ is a sufficiently good approximation for the sources displayed in Fig. 12, given that higher ΔV (as in Arp 220W) would be partially compensated by a lower $X_{\text{HCN}}/\Delta V$ if X_{HCN} is nearly independent of ΔV . The range of solid angles that we estimate for the sources is discussed below in detail (§3.2.5) and listed in Table 2.

Each hatched colored region in Fig. 12 indicates model results for a given Σ_{IR} , delimited by AGN (open circles) and SB (starred symbols) models. In panel b, the flux ratio of the HCN $\nu_2 = 1^f J = 4-3$ to the $\nu_2 = 1^f J = 3-2$ lines is plotted for the same models as in the left-hand panel, and compared with available data as well (see §3.2.5).

For moderate columns, the dependence of $F_{\text{HCN}\nu_{23-2}}/\Delta\Omega$ on N_{H_2} is supralinear, because of the increase of both T_{dust} and N_{HCN} as N_{H_2} rises. However, the dependence becomes sub-linear for $N_{\text{H}_2} > 5 \times 10^{24} \text{ cm}^{-2}$ and $\Sigma_{\text{IR}} > 10^8 L_\odot \text{ pc}^{-2}$, and the curves flatten at the highest N_{H_2} . At these extreme values, the HCN vibrational emission is optically thick over most of the continuum source. At the highest $N_{\text{H}_2} = 10^{19} \text{ cm}^{-2}$ (i.e. $N_{\text{H}_2} = 10^{25} \text{ cm}^{-2}$) we consider in this work, the flux ratio $\nu_2 = 1^f J = 4-3/3-2$ is lower than the optically thick limit because of the enhanced absorption of the continuum by the $\nu_2 = 1^f J = 4-3$ line (see Fig. 10d-e for a comparison of the $\nu_2 = 1^f J = 3-2$ and $J = 4-3$ optical depths). The use of the black κ_ν -curve of Fig. 1 would increase the calculated ratios to values closer to the optically thick limit of 1.8, and the values of $F_{\text{HCN}\nu_{23-2}}/\Delta\Omega$ would also increase by $\sim 25\%$ at $N_{\text{H}_2} = 10^{25} \text{ cm}^{-2}$ (results for lower N_{H_2} are more similar).

The dependence of $F_{\text{HCN}\nu_{23-2}}/\Delta\Omega$ on N_{H_2} in Fig. 12 becomes steeper as N_{H_2} and Σ_{IR} decrease, and more so for SB models. This effect is partially due to the adopted density

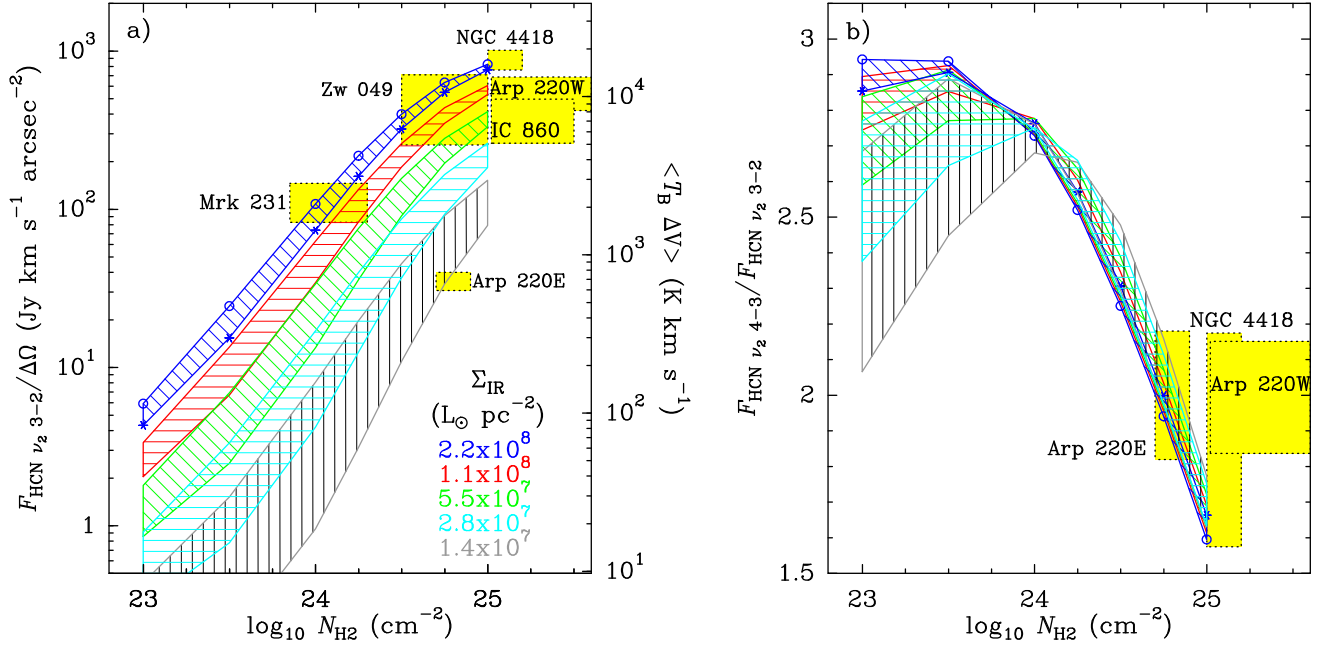


Figure 12. a) The flux of the HCN $\nu_2 = 1^f J = 3-2$ line per unit of solid angle of the source, as a function of the H_2 column density. The right-hand axis gives the source-averaged velocity-integrated brightness of the line. Each hatched region corresponds to a value of the continuum surface brightness Σ_{IR} as indicated, and is delimited by AGN (higher values) and SB (lower values) models. Other model parameters have fiducial values ($q = 1$, $R_{\text{out}}/R_{\text{int}} = 17$, $X_{\text{HCN}}/\Delta V = 1.5 \times 10^{-8} (\text{km s}^{-1})^{-1}$, $\Delta V = 67 \text{ km s}^{-1}$). b) The HCN $\nu_2 = 1^f J = 4-3$ to $\nu_2 = 1^f J = 3-2$ flux ratio, both in Jy km s^{-1} , for the same models as in the left-hand panel. The yellow rectangles indicate the most plausible ranges for both axis in several galaxies (see §3.2.5).

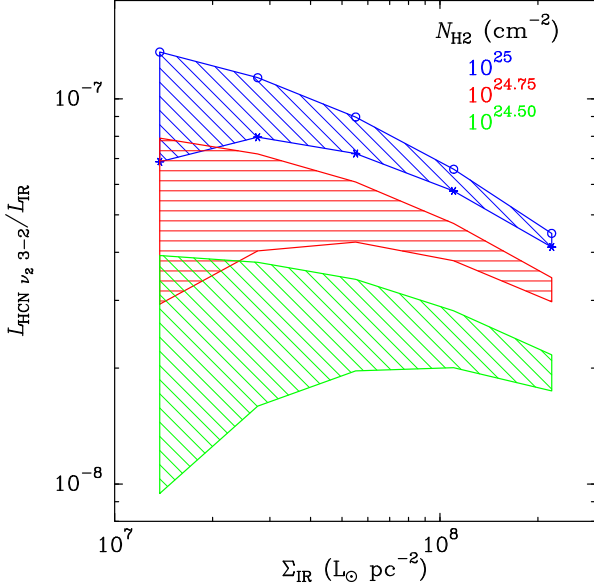


Figure 13. The ratio of the HCN $\nu_2 = 1^f J = 3-2$ luminosity to the infrared luminosity of the source, as a function of Σ_{IR} . Each hatched region corresponds to a value of the H_2 column density as indicated, and is delimited by AGN (higher values) and SB (lower values) models. Other model parameters have fiducial values ($q = 1$, $R_{\text{out}}/R_{\text{int}} = 17$, $X_{\text{HCN}}/\Delta V = 1.5 \times 10^{-8} (\text{km s}^{-1})^{-1}$, $\Delta V = 67 \text{ km s}^{-1}$).

profiles. As shown in §3.2.1 for the $Q(3)$ transition, the rovibrational HCN lines at $14 \mu\text{m}$ are thermalized to T_{dust} , so that the excitation of the $\nu_2 = 1^f J = 3-2$ and $J = 4-3$ lines mimics the excitation of the corresponding $\nu = 0$ transitions (Fig. 8). In regions with $T_{\text{dust}} \gtrsim 200 \text{ K}$, radiative excitation is enough to keep the $\nu = 0 J = 3-2$ and $4-3$ nearly thermalized at $T_{\text{EX}} = T_{\text{dust}} = T_{\text{gas}}$ even for low N_{H_2} , but the line excitation in both vibrational states becomes subthermal for lower T_{dust} (Fig. 8d,f). Therefore, if the densities were higher than in our models (Fig. 7), the dependence of $F_{\text{HCN } \nu_{23-2}}/\Delta\Omega$ on N_{H_2} would not be as steep as in Fig. 12 for low Σ_{IR} . This also explains the turnaround seen in Fig. 12b in the $\nu_2 = 1^f 4-3/3-2$ flux ratio, as the subthermal excitation affects more deeply the $4-3$ line than the $3-2$ transition. If the densities were higher, the turnaround of the $\nu_2 = 1^f 4-3/3-2$ flux ratio with decreasing N_{H_2} would not be so pronounced. For the highest N_{H_2} considered, however, our HCN fluxes are maximum and no higher values would be obtained with higher adopted densities (for our fiducial values).

Therefore, the values of $L_{\text{HCN } \nu_{23-2}}/L_{\text{IR}}$ shown in Fig. 13 are also maximum for our adopted fiducial parameters and continuum opacity at 1.1 mm ⁷. For fixed N_{H_2} and high Σ_{IR} ,

⁷ Somewhat higher values would be obtained with the black κ_{ν} -curve of Fig. 1 as the optical depth and continuum brightness at 1.1 mm would be lower and thus the effect of absorption of this continuum by the HCN

$L_{\text{HCN}\nu_{23-2}}/L_{\text{IR}}$ drops with increasing Σ_{IR} . This is because a further increase of Σ_{IR} is not followed by a proportional increase of $\Delta\Omega_{\tau=1}$ (eq. 5), and produces in addition brighter millimeter continuum emission and thus more absorption by the HCN line. Both $L_{\text{HCN}\nu_{23-2}}$ and L_{IR} are calculated in spherical symmetry but both are optically thick, so that the ratio of the apparent luminosities is probably valid for more general geometries. In general, the BGN infrared luminosity is a fraction of the L_{IR} of the host galaxy, but the vast majority of the HCN vibrational emission arises from the nucleus –unless the galaxy has other off-nuclear, buried sources. Hence, the $L_{\text{HCN}\nu_{23-2}}/L_{\text{IR}}$ values for the nucleus plotted in Fig. 13 are upper limits to the corresponding ratios for the entire galaxy.

3.2.5. Comparison with data

As stated above, $\Delta\Omega = \pi R_{\text{out}}^2/D^2$ in Fig. 12a is the solid angle of the cocoon covering the luminosity source(s), rather than of the less extended HCN vibrational emission, so that comparison with data can be performed even if the HCN $\nu_2 = 1$ lines are spatially unresolved. However, the radius R_{out} of the cocoon over which the luminosity of the embedded sources is reemitted, must be estimated. In buried sources, the luminosity is mainly emitted at far-IR wavelengths (Fig. 2b), for which a nearly flat profile is found (Fig. 11a); therefore, R_{out} can be empirically defined as the radius of the far-IR source. The caveat is that the far-IR extent may be underestimated by measurements of millimeter-wave continuum, which is strongly peaked toward the center (Fig. 11a). In principle, interferometric measurements at shorter (submillimeter) wavelengths are better suited to probe the source extent. Alternatively, $\Delta\Omega$ can be estimated from the analysis of high-lying far-IR molecular absorption⁸, as these lines are directly probing the far-IR photosphere and thus the full extent of the source. On the other hand, spatially extended continuum unassociated directly with the source of HCN vibrational emission should be ignored. A suitable criterion would be to exclude surrounding regions where the inferred H_2 column density translates into optically thin far-IR emission (i.e. $< 5 \times 10^{23} \text{ cm}^{-2}$), as the greenhouse effect no longer takes place. We only consider in the following sources with HCN vibrational emission where $\Delta\Omega$ can be reasonably estimated.

Analysis of interferometric measurements usually involve Gaussian curves to fit sizes; to compare with our spherical models, we use the equivalent size of a uniform disk, i.e.

line (§3.2.3) would be less important. The increase of ΔV would also boost $L_{\text{HCN}\nu_{23-2}}/L_{\text{IR}}$.

⁸ The extremely buried nuclei are best traced by far-IR molecular lines with $E_{\text{low}} > 500 \text{ K}$, such as the $\text{H}_2\text{O } 7_{07-6_{16}}$ at $72 \mu\text{m}$; low-lying lines usually probe in addition more extended, colder components with lower column densities.

$R_{\text{out}} = 0.8 \times \text{FWHM}$ (Appendix A in Sakamoto et al. 2008). The values of $\Delta\Omega$ for all individual sources used in Fig. 12, listed in Table 2 together with the inferred Σ_{IR} , L_{IR} , and T_{dust} throughout the far-IR photosphere, are justified in continuation.

NGC 4418: an extremely compact and warm source of far-IR emission was identified from the strong and very excited molecular lines of H_2O , OH, and other species including HCN (González-Alfonso et al. 2012). The radius of this source was estimated to be $\approx 10 \text{ pc}$ at an adopted $D = 29 \text{ Mpc}$, i.e. $\Delta\Omega = 1.6 \times 10^{-2} \text{ arc sec}^2$. From high-angular resolution observations at $\approx 350 \text{ GHz}$, Sakamoto et al. (2013) estimated a radius of $\approx 13.5 \text{ pc}$ at an adopted $D = 34 \text{ Mpc}$, i.e. $\Delta\Omega = 2.1 \times 10^{-2} \text{ arc sec}^2$. We have used these two values of $\Delta\Omega$ and a flux of the HCN line of 16 Jy km s^{-1} (Sakamoto et al. 2010) to give $F_{\text{HCN}\nu_{23-2}}/\Delta\Omega = 760-1000 \text{ Jy km s}^{-1} \text{ arc sec}^{-2}$. Only the maximum value of $\Sigma_{\text{IR}} = 2.2 \times 10^8 \text{ L}_{\odot} \text{ pc}^{-2}$ can account for this brightness (Fig. 12), yielding a source luminosity of $D^2 \Delta\Omega \Sigma_{\text{IR}} = (0.9-1.3) \times 10^{11} \text{ L}_{\odot}$. This estimate agrees with the conclusion that the bulk of the galaxy luminosity emerges from such a compact region (González-Alfonso et al. 2012; Sakamoto et al. 2013). In addition, our continuum models for $\Sigma_{\text{IR}} = 2.2 \times 10^8 \text{ L}_{\odot} \text{ pc}^{-2}$ predict $T_{\text{dust}} = 115-160 \text{ K}$ for the photosphere with $\tau_{60\mu\text{m}} \leq 0.5$ from the surface (Table 2), in general agreement with requirements to account for the high-lying molecular absorption in the far-IR (González-Alfonso et al. 2012). The HCN $\nu_2 = 1^f J = 4-3$ to $J = 3-2$ flux ratio of 1.9 ± 0.3 (Sakamoto et al. 2010) is also consistent with strongly saturated HCN vibrational emission.

Arp 220W: the western nucleus of Arp 220 has been recently imaged with extremely high angular resolution at (sub)millimeter wavelengths. Visibility fitting of the 3 mm continuum by Sakamoto et al. (2017) shows that a 2 Gaussian fitting (or 1 Gaussian and 1 exponential disk) performs much better than a single Gaussian. While the 3 mm emission from the compact source, with an equivalent $R_{\text{out}} = 14 \text{ pc}$, is dominated by thermal dust emission, the emission from the larger component, with $R_{\text{out}} = 60 \text{ pc}$, is predominantly non-thermal. At the higher frequency of 691 GHz, Wilson et al. (2014) infer $R_{\text{out}} \leq 80 \text{ pc}$, and in the far-IR González-Alfonso et al. (2012) estimate $R_{\text{out}} = 47-89 \text{ pc}$ (both corrected for a distance of 85 Mpc). For the reason stated above, the more extended component at 3 mm is probably emitting in the far-IR, so that we adopt $R_{\text{out}} = 47-60 \text{ pc}$ yielding $\Delta\Omega = (4.1-6.7) \times 10^{-2} \text{ arc sec}^2$. With the HCN flux of $\sim 28 \text{ Jy km s}^{-1}$ (Martín et al. 2016), $F_{\text{HCN}\nu_{23-2}}/\Delta\Omega = 400-700 \text{ Jy km s}^{-1} \text{ arc sec}^{-2}$. This is significantly lower than the brightness of the line in NGC 4418, in agreement with the significantly lower excitation of the far-IR absorption lines in Arp 220, and can

Table 2. Estimated solid angles $\Delta\Omega$ for the BGNs considered in §3.2.5, line fluxes of the HCN vibrational lines, and inferred values of Σ_{IR} , L_{IR} , and T_{dust} at the far-IR photosphere

Source	D_L (Mpc)	R_{out} (pc)	$\Delta\Omega$ (10^{-2} arc sec 2)	Ref ^a	$F_{\text{HCN } \nu_{23-2}}$ (Jy km s $^{-1}$)	$F_{\text{HCN } \nu_{24-3}}$ (Jy km s $^{-1}$)	Ref ^b	Σ_{IR} ($10^7 L_{\odot}$ pc $^{-2}$)	L_{IR} ($10^{11} L_{\odot}$)	$T_{\text{dust-photo}}$ (K)
(1)	(2)	(3)	(4)	(5)	(6)	(7)	(8)	(9)	(10)	(11)
NGC 4418	34	11.7–13.5	1.6–2.1	1,2	16	30	3	22	0.9–1.3	115–160
Arp 220W	85	47–60	4.1–6.7	1,4,5	28	55.0	6	11	7.6–12	100–130
Arp 220E	85	87–90	14–15	4,5	5.1	10.2	6	0.5–1	1.3–2.4	50–65
Zw 049.057	56	15–25	1.0–2.7	7	6.8		8	5–20	1.0–1.4	80–160
IC 860	59	14.5–20	0.8–1.5	11	4		8	5.5	0.4–0.7	80–105
Mrk 231	192	55–73	1.1–1.9	9	1.6		10	11–22	18–21	95–180

NOTE—(1) Galaxy name; (2) Luminosity distance; (3) Estimate for the outer radius of the cocoon reemitting the luminosity generated by the embedded source(s), based on both the measured sizes in the (sub)millimeter and on the calculated sizes from far-IR molecular absorption (see text); (4) Solid angle, calculated as in Table 1; (5) References for R_{out} ; (6) Flux of the HCN $\nu_2 = 1^f J = 3-2$ line; (7) Flux of the HCN $\nu_2 = 1^f J = 4-3$ line; (8) References for the HCN $\nu_2 = 1^f$ fluxes; (9) Estimated value of Σ_{IR} based on the location of sources in Fig. 12a; (10) Luminosity of the BGN, calculated as $L_{\text{IR}} = \Sigma_{\text{IR}} \Delta\Omega D_L^2$; (11) Range of T_{dust} values throughout the far-IR photosphere, defined as $\tau_{60\mu\text{m}} \leq 0.5$ from the surface, as predicted by the best-fit continuum models.

References: (1) González-Alfonso et al. (2012) (2) Sakamoto et al. (2013) (3) Sakamoto et al. (2010) (4) Sakamoto et al. (2017) (5) Wilson et al. (2014) (6) Martín et al. (2016) (7) Falstad et al. (2015) (8) Aalto et al. (2015b) (9) González-Alfonso et al. (2014b) (10) Aalto et al. (2015a) (11) Aalto et al. (2019)

be explained with $\Sigma_{\text{IR}} = 1.1 \times 10^8 L_{\odot} \text{pc}^{-2}$ (Fig. 12a)⁹. The implied luminosity is $(0.76-1.2) \times 10^{12} L_{\odot}$, in good agreement with the luminosity inferred from the analysis of the far-IR absorption lines $((0.91-1.1) \times 10^{12} L_{\odot}$ after correcting for the adopted distance; González-Alfonso et al. 2012). For $\Sigma_{\text{IR}} = 1.1 \times 10^8 L_{\odot} \text{pc}^{-2}$, the predicted T_{dust} across the $\tau_{60\mu\text{m}} \leq 0.5$ photosphere is 100–130 K, also in agreement with the inferred values from the far-IR absorption lines. We also favor the AGN model that predicts high central continuum brightness T_{B} in the millimeter, in excess of 500 K for $N_{\text{H}_2} \sim 10^{26} \text{cm}^{-2}$ (Fig. 11b), similar to the value measured by Sakamoto et al. (2017); by contrast, the SB model for the same value of Σ_{IR} yields maximum brightness of ≈ 400 K. The main drawback of our model is that it predicts a low HCN $\nu_2 = 1^f J = 4-3$ to $J = 3-2$ flux ratio of $\lesssim 1.7$ owing to the extreme column densities, while the observed value is 2.0 ± 0.16 (Martín et al. 2016).

Arp 220E: the eastern nucleus of Arp 220 has been also imaged with high angular resolution in the (sub)millimeter.

⁹ As noted in §3.2.4, the modeled $F_{\text{HCN } \nu_{23-2}}/\Delta\Omega$ would have to be multiplied by $\Delta V/(67 \text{ km s}^{-1})$, with the result that the observed value could be explained with even lower Σ_{IR} for the high ΔV inferred from CO observations (Scoville et al. 2017), although we also note that ΔV would have to be corrected by optical depth broadening and that a lower $X_{\text{HCN}}/\Delta V$ would also partially compensate for the increase of ΔV .

Sakamoto et al. (2017) found $\Delta\Omega = 0.14 \text{ arc sec}^2$ at 3 mm (i.e. $R_{\text{out}} = 87 \text{ pc}$ for the extended component), and Wilson et al. (2014) determined $\Delta\Omega = 0.15 \text{ arc sec}^2$ at $434 \mu\text{m}$. Using the HCN flux of $4.6-5.6 \text{ Jy km s}^{-1}$ by Martín et al. (2016), we infer $F_{\text{HCN } \nu_{23-2}}/\Delta\Omega = 30-40 \text{ Jy km s}^{-1} \text{ arc sec}^{-2}$. On the other hand, the HCN $\nu_2 = 1^f J = 4-3$ to $J = 3-2$ flux ratio is 2.0 ± 0.2 (Martín et al. 2016), consistent with $N_{\text{H}_2} \sim 10^{24.8} \text{ cm}^{-2}$. Our model with the minimum $\Sigma_{\text{IR}} = 1.4 \times 10^7 L_{\odot} \text{pc}^{-2}$ may still overestimate the line brightness, so that we adopt $(0.5-1) \times 10^7 L_{\odot} \text{pc}^{-2}$ yielding a luminosity of $(1.3-2.4) \times 10^{11} L_{\odot}$ at 85 Mpc, consistent with the estimate by Wilson et al. (2014).

IC 860: Recent interferometric observations have revealed an extremely compact source at (sub)millimeter wavelengths, with equivalent $R_{\text{out}} = (13-14.5) \text{ pc}$ (Aalto et al. 2019); however, the HCN $\nu_2 = 1^f J = 3-2$ line is more extended, $R_{\text{out}} \approx 20 \text{ pc}$, suggesting that the infrared emission has at least a similar size. We have nevertheless adopted the conservative range $R_{\text{out}} = (14.5-20) \text{ pc}$ and thus $\Delta\Omega = (0.8-1.5) \times 10^{-2} \text{ arc sec}^2$. Using the HCN flux of $\approx 4 \text{ Jy km s}^{-1}$ by Aalto et al. (2015b), we infer $F_{\text{HCN } \nu_{23-2}}/\Delta\Omega = 260-500 \text{ Jy km s}^{-1} \text{ arc sec}^{-2}$, which is mostly consistent with $\Sigma_{\text{IR}} \sim 5.5 \times 10^7 L_{\odot} \text{pc}^{-2}$ (Fig. 12a). The infrared luminosity of the nucleus is then $(4-7) \times 10^{10} L_{\odot}$, 30–50% of the total infrared luminosity of the galaxy.

Zw 049.057: An obscured and compact nucleus was identified by Falstad et al. (2015) from high-lying far-IR molecular absorption, with a most plausible radius of 15–25 pc at 56 Mpc ($\Delta\Omega = (1.0–2.7) \times 10^{-2}$ arc sec²) and a column density of $N_{\text{H}_2} \sim 10^{24.5–25}$ cm⁻². The HCN $\nu_2 = 1^f J = 3–2$ line was detected by Aalto et al. (2015b) with a flux of 6.8 Jy km s⁻¹, yielding 250–700 Jy km s⁻¹ arc sec⁻². From Fig. 12, we estimate $\Sigma_{\text{IR}} = (0.5–2) \times 10^8 L_{\odot} \text{pc}^{-2}$ for the upper and lower limit of $\Delta\Omega$, respectively. This gives a luminosity of $(1.0–1.4) \times 10^{11} L_{\odot}$ for the compact core, in agreement with the estimate by Falstad et al. (2015) from far-IR molecular absorption lines ($(0.7–1.2) \times 10^{11} L_{\odot}$). Our predicted range of T_{dust} across the far-IR photosphere brackets the range favored by Falstad et al. (2015) (90–130 K).

Mrk 231: A highly excited component was inferred from high-lying OH absorption in the far-IR (González-Alfonso et al. 2014b), with an estimate radius of 55–73 pc at 192 Mpc. We thus adopt $\Delta\Omega = (1.1–1.9) \times 10^{-2}$ arc sec², which with the observed HCN flux of 1.6 Jy km s⁻¹ (Aalto et al. 2015a) yields $F_{\text{HCN } \nu_{23-2}}/\Delta\Omega = 80–150$ Jy km s⁻¹ arc sec⁻². This component is not expected to have the extremely high column densities of the previous sources, but $N_{\text{H}_2} \sim (0.7–2) \times 10^{24}$ cm⁻² (González-Alfonso et al. 2014b). This is consistent with a high $\Sigma_{\text{IR}} = (1.1–2.2) \times 10^8 L_{\odot} \text{pc}^{-2}$ (Fig. 12), which translates into a luminosity of $(1.8–2.1) \times 10^{12} L_{\odot}$, the expected luminosity of the nucleus. Our range of photospheric T_{dust} in Table 2 includes the values favored from far-IR molecular absorption (95–120 K, González-Alfonso et al. 2014), and suggests that the model with lower $\Sigma_{\text{IR}} \sim 10^8 L_{\odot} \text{pc}^{-2}$ (with $T_{\text{dust}} - \text{photo} = 100–135$ K) better fits the data. The HCN $\nu_2 = 1^f J = 4–3$ line has not been observed, and our model predicts a $\nu_2 = 1^f J = 4–3$ to $J = 3–2$ flux ratio significantly higher than for the other sources, ~ 2.5 .

4. DISCUSSION

The greenhouse effect presented here, or the effect of increasing dust temperatures due to trapping of mid- and far-IR radiation in environments of extreme column densities, has the advantage of explaining, through the calibration presented in Fig. 12, three general observations: the bright emission of the HCN vibrational lines in buried sources, the dust temperatures in the photosphere required to explain the high-lying molecular absorption in the far-IR, and the high brightness and compactness of the (sub)millimeter continuum, all with involved source luminosities that are consistent with values calculated from independent approaches.

As pointed out in §2.1, our models are in principle applicable to a single source or to an ensemble of non-radiatively interacting sources. However, luminous HCN vibrational emission in well-studied cases is arising from well defined compact galactic nuclei rather than from individual giant molecular clouds (GMCs) widespread over a kilo-parsec disk, even

though “hot cores” in our galaxy also show HCN $\nu_2 = 1$ emission. There are probably several reasons that can account for this. First, the values of $\Sigma_{\text{IR}} \sim 10^8 L_{\odot} \text{pc}^{-2}$ we infer in the most buried BGNs are higher than the values $\lesssim 10^6 L_{\odot} \text{pc}^{-2}$ typically inferred in galactic hot cores (e.g. Nomura & Millar 2004; Doty et al. 2006), although in some cases $\Sigma_{\text{IR}} \gtrsim 10^7 L_{\odot} \text{pc}^{-2}$ (Cesaroni et al. 2010). In addition, the timescale of this buried phase in individual clouds, $\sim 10^5$ yr (e.g. Wilner et al. 2001; Doty et al. 2006), is much shorter than the typical dynamical time scale of galactic disks. When the buried phase turns on in independent clouds, their appearance is spread out over the full dynamical timescale of the disk and their contribution to the luminosity of the galaxy will be low. In galaxies where high HCN vibrational fluxes are detected, the synchronization required by large gas masses participating in the buried phase can only take place within a common sphere of influence, the galactic nucleus. This accounts for the bimodality observed in the high-lying OH 65 μm absorption in galaxies, suggesting “coherent” structures (González-Alfonso et al. 2015). Finally, in case of multiple luminosity sources, the greenhouse effect and HCN vibrational excitation should be generally more enhanced when the sources are packed and radiatively coupled with each other than when they are widespread and radiatively decoupled. This is because packed sources have mutual heating and mutual contribution to the overall shielding required for an efficient greenhouse effect. The gas velocity dispersion ΔV is also higher in this latter scenario, contributing to further boost the HCN vibrational emission.

The spherical symmetry used in the present study, however, assumes isotropic column densities from the center and no clumpiness. This oversimplified smoothed density structure may overestimate the dust temperature as compared with real systems. If the gas and dust are mainly concentrated into clumps, there will be an increasing number of sightlines with lower column densities along which the radiation tends to escape (e.g. Roth et al. 2012), decreasing T_{dust} . Likewise, a flat structure like a disk will have minimum column densities along the direction perpendicular to the disk plane, and radiation will tend to escape in that direction. We have indeed evidence for a clumpy structure in the galaxies considered in this work, as the analysis of the HCN band at 14 μm yields excitation temperatures of ~ 300 K (Lahuis et al. 2007) while the photosphere in our models has temperatures significantly lower. In addition, most individual sources considered here (Arp 220, NGC 4418, Zw 049.057, and IC 860) are estimated to have $N_{\text{H}_2} > 10^{24.5}$ cm⁻², for which our AGN models predict little—but observations show prominent—9.7 μm absorption. The mid-IR continuum in front of which the silicate absorption is produced is arising from regions at 350–400 K (González-Alfonso et al. 2012), clearly warmer than the T_{dust} at the far-IR photosphere of our models. This continuum may

be due to leakage of mid-IR radiation from the very nuclear region, or generated by a surrounding star formation component. Judging from the SED of NGC 4418, where the output power is most likely dominated by the BGN, the leakage of mid-IR radiation is estimated as $L_{5-20\mu\text{m}}/L_{5-1000\mu\text{m}} \approx 10\%$, although part of the mid-IR emission may arise from surrounding super star clusters as observed with VLBI at radio wavelengths (Varenius et al. 2014).

The caveat here is the contrast between the column densities through clumps and along sightlines that only cross interclump material –the background smooth gas distribution. At least in the innermost nuclear regions of the galaxies considered in this work, clouds are expected to (partially) lose their individuality and blend into a fluctuating-dense medium (e.g. Scoville et al. 1997; Downes & Solomon 1998). We also note that the column densities of $\gtrsim 10^{25} \text{ cm}^{-2}$ inferred in the nuclear regions of (U)LIRGs where HCN vibrational emission is detected are beam-averaged, and thus high columns apply to a significant range of solid angles –unless the nucleus is seen close to edge on. If these compact nuclei are mainly supported by radiation pressure, the rotation will slow down and the inner disk will evolve to become more spheroidal, like a cocoon with high columns even in the polar direction¹⁰. Viewing the problem with a different perspective, and considering the high HCN abundance that is still required to explain the HCN $\nu_2 = 1$ emission, one could hypothesize that strong HCN vibrational emission arises only in galaxies where the greenhouse effect turns on as a result of the high column densities averaged over solid angles. By contrast, in galaxies where OH shows prominent outflows that are expected to be wide-angle, the column densities averaged over solid angles will be significantly lower due to sweeping out the nuclear ISM by the outflow, and the greenhouse effect will also be much less important with the consequent weakness of the HCN vibrational emission (Falstad et al. 2019).

When the column densities averaged over solid-angles become so large that the region becomes opaque to its own mid- and even far-IR emission, the increase of T_{dust} is unavoidable. As the temperature increases, the dust emits at shorter wavelengths for which the optical depths are even higher, thus enhancing the radiation trapping effect. With $\tau_{20\mu\text{m}} \sim 300$ for $N_{\text{H}_2} = 10^{25} \text{ cm}^{-2}$ (Fig. 2a), $20 \mu\text{m}$ photons have negligible probability to escape and the radiation field becomes nearly isotropic. The interior of BGNs are infrared-dominated regions.

Our calibration in Fig. 12 implies source luminosities that are in agreement, for all sources considered in this paper, with independent estimates (§3.2.5). The calibration involves

a high $X(\text{HCN}) \approx 10^{-6}$, in rough agreement with the value inferred in the far-IR photosphere of NGC 4418 from HCN rotational lines seen in absorption (González-Alfonso et al. 2012) and with the values inferred from the HCN $14 \mu\text{m}$ band (Lahuis et al. 2007). Nevertheless, the effect of $X(\text{HCN})$ in our model calculation is coupled with the effects of other fiducial parameters, such as q , ΔV , and the κ -curve (Fig. 1). Allowing for the possible errors in these parameters, we estimate that the fiducial $X(\text{HCN})$ is probably accurate within a factor ~ 2 for $T_{\text{dust}} \gtrsim 200 \text{ K}$. On the one hand, the general chemical picture depicted by Harada et al. (2010) is supported here, in the sense that high temperatures lock an important fraction of oxygen into hydrides like H_2O and OH , as observed in the far-IR, leaving an effective carbon-rich gas-phase chemistry that boosts the abundances of cyanopolynes. On the other hand, the abundance of HCN in the chemical models drops quickly for $T_{\text{gas}} < 400 \text{ K}$, while we favor a high HCN abundance down to at least $T_{\text{dust}} \sim 200 \text{ K}$. It is possible that generalized shock chemistry keeps a substantial fraction of the gas in the external regions of the cocoons with $T_{\text{gas}} > T_{\text{dust}}$.

The involved HCN column densities are so high in BGNs that it becomes hard, at least from our starburst approach, to distinguish between AGN-dominated and SB-dominated regions from the observed HCN $\nu_2 = 1^f J = 3-2$ and $4-3$ lines alone. Nevertheless, high-resolution observations of these lines provide very useful constraints on the spatial extent where the greenhouse effect turns on, and on the velocity field of the gas in the inner regions that could provide evidence for a central point-like concentration of mass. If Σ_{IR} can be estimated from these observations, as performed in §3.2.5 and including spatial information if the lines are resolved, high-resolution observations of the (sub)millimeter continuum would provide the peak brightness and then favor an AGN or SB origin of the luminosity. The very strong brightness peak at 2.6 mm in Arp 220W (Sakamoto et al. 2017), combined with our inferred $\Sigma_{\text{IR}} \sim 10^8 L_{\odot} \text{ pc}^{-2}$ and the high point-like mass concentration (Scoville et al. 2017), allow us to favor an energetically significant AGN in this source.

In general, discriminating between an AGN or SB origin of the luminosity relies on the upper value that Σ_{IR} could attain in a compact starburst; we do not rule out that starbursts even more compact and intense than considered in this study are possible. For the highest $N_{\text{H}_2} = 10^{25} \text{ cm}^{-2}$ considered in this work, $\Sigma_{\text{IR}} \gtrsim 2 \times 10^8 L_{\odot} \text{ pc}^{-2}$ makes AGN and SB models basically indistinguishable upon the diagnostics considered here, assuming that this value is physically possible for a starburst. On the other hand, convective energy transfer can make the T_{dust} distribution of an AGN closer to that of a SB. We also note that the most deeply buried BGNs ($N_{\text{H}_2} > 10^{25} \text{ cm}^{-2}$) have photon-diffusion timescales

¹⁰ This effect, combined with the inferred expansion of the nuclear regions in ULIRGs (González-Alfonso et al. 2017), may be crucial for the formation of spheroidal bulges.

($\gtrsim 10^4$ yr) that are similar to the flickering time of quasar-like AGN (10^{4-5} yr; e.g. Schawinski et al. 2015; Ichikawa et al. 2019), so that an AGN-powered BGN with high IR luminosity can have a faded AGN at its center. In such a case, even if the BGN cocoon around the AGN has a small gap, we may see little AGN signature in the leaked short-wavelength radiation. In BGNs, an AGN may resemble a SB if these effects become significant.

5. CONCLUSIONS

We have modeled in spherical symmetry both the T_{dust} profile and the HCN vibrational emission, with special emphasis in models with high column densities, to be applied to the nuclear region of buried galaxies. Both AGN and starburst models have been generated. Our main findings are:

1. Trapping of the continuum radiation at mid- and far-infrared wavelengths extraordinarily increases the dust temperatures in the innermost regions of the modeled sources. This greenhouse effect enhances by more than one order of magnitude the radiation density in the mid-IR responsible for the vibrational excitation of the cyanopolynes.
2. The increase of T_{dust} in the innermost regions is capable of generating continuum brightness of several hundred K at millimeter wavelengths in sources where the optical depth at these frequencies becomes significant.
3. The models for the continuum also predict dust temperatures close to the surface of the source, i.e. at the far-IR photosphere, that are in agreement with those required to explain the high-lying far-IR molecular absorption observed with *Herschel*/PACS in the most buried and warmest sources.
4. We use the results of the continuum models to calculate the excitation and emission of HCN from the $J = 3-2$ and $4-3$ lines of the bending ($\nu_2 = 1$) vibrational state. The vibrationally excited lines are much more useful than the ground-state ($\nu = 0$) lines to look deeper inside the hot, obscured galactic nuclei.
5. For the highest column density we have considered, $N_{\text{H}_2} = 10^{25} \text{ cm}^{-2}$, the above HCN lines are optically

thick at least in the innermost regions for luminosity surface densities above $\Sigma_{\text{IR}} \sim 10^7 L_{\odot} \text{ pc}^{-2}$. The radius of this HCN $\nu_2 = 1$ photosphere increases with increasing Σ_{IR} .

6. For sufficiently high column densities, which we estimate to be $10^{25} - 10^{25.5} \text{ cm}^{-2}$, we expect a drop of the brightness of the HCN vibrational lines toward the center of the source, due to line absorption of the bright (sub)millimeter continuum.
7. Using the abundance $X(\text{HCN}) = 10^{-6}$ and an intrinsic $\Delta V = 67 \text{ km s}^{-1}$, we reproduce the observed brightness of the HCN vibrational lines in several galaxies, with inferred luminosities that agree with independent estimates.
8. The HCN $\nu_2 = 1^f J = 3-2$ and $J = 4-3$ lines have significant optical depths in buried sources, and the impact of very high T_{dust} in AGN models is moderate on the populations of the involved low- J levels. Nevertheless, the combination with high-resolution measurements of the (sub)millimeter continuum and dynamical estimates of the central mass can provide useful diagnostics to favor an AGN or starburst origin of the source luminosity.

We thank Francesco Costagliola for his help in writing scripts to generate models sequentially, and an anonymous referee for useful comments that improved the manuscript. We thank Susanne Aalto for enabling us to use the data of IC 860 prior to the publication, and to participants at the Sesto 2019 workshop for comments on this work, in particular Dr. Jay Gallagher for his question on convection in BGNs. E.G.A. is a Research Associate at the Harvard-Smithsonian Center for Astrophysics, and thanks the Spanish Ministerio de Economía y Competitividad for support under project ESP2017-86582-C4-1-R. KS acknowledges the grant-in-aid MOST 107-2119-M-001-022. This research has made use of NASA's Astrophysics Data System (ADS) and of GILDAS software (<http://www.iram.fr/IRAMFR/GILDAS>).

Software: GILDAS

REFERENCES

- Aalto, S., García-Burillo, S., Muller, S., et al. 2012, *A&A*, 537, 44
Aalto, S., García-Burillo, S., Muller, S., et al. 2015a, *A&A*, 574, A85
Aalto, S., Martín, S., Costagliola, F., et al. 2015b, *A&A*, 584, A42
Aalto, S., et al. in prep. 2019
Aladro, R., König, S., Aalto, S., et al. 2018, *A&A*, 617, A20
Andrews, B. H., & Thompson, T. A. 2011, *ApJ*, 727, 97
Cesaroni, R., Hofner, P., Araya, E., & Kurtz, S. 2010, *A&A*, 509, A50
Chang, Y.Y., Le Floch, E., Juneau, S., et al. 2017, *MNRAS*, 466, L103
Costagliola, F., & Aalto, S. 2010, *A&A*, 515, A71

- Costagliola, F., Aalto, S., Sakamoto, K., Martín, S., Beswick, R., Muller, S., & Klöckner, H.-R. 2013, *A&A*, 556, A66
- Dekel, & Burkert 2014
- Doty, S. D., van Dishoeck, E. F., & Tan, J. C. 2006, *A&A*, 454, L5
- Downes, D., & Solomon, P. M. 1998, *ApJ*, 507, 615
- Draine, B.T. 2003, *Annu. Rev. Astr. Astrophys.*, 41, 241
- Dumouchel, F., Faure, A., & Lique, F. 2010, *MNRAS*, 406, 2488
- Falstad, N., González-Alfonso, E., Aalto, S., van der Werf, P. P., Fischer, J., Veilleux, S., Meléndez, M., Farrah, D., & Smith, H. A. 2015, *A&A*, 580, A52
- Falstad, N., González-Alfonso, E., Aalto, S., & Fischer, J., 2017, *A&A*, 597, A105
- Falstad, N., Aalto, S., Mangum, J. G., et al. 2018, *A&A*, 609, A75
- Falstad, N., Hallqvist, F., Aalto, S., et al. 2019, *A&A*, in press
- Faucher-Giguère, C.-A. & Quataert, E. 2012, *MNRAS*, 425, 605
- Förster Schreiber, N. M., Genzel, R., Lutz, D., & Sternberg, A. 1993, *ApJ*, 599, 193
- García-Burillo, S., Combes, F., Usero, A., et al. 2015, *A&A*, 580, A35
- González-Alfonso, E., & Cernicharo, J. 1997, *A&A*, 322, 938
- González-Alfonso, E., & Cernicharo, J. 1999, *ApJ*, 525, 845
- González-Alfonso, E., Smith, H. A., Fischer, J., & Cernicharo, J. 2004, *ApJ*, 613, 247
- González-Alfonso, E., Fischer, J., Graciá-Carpio, J., et al. 2012, *A&A*, 541, A4
- González-Alfonso, E., Fischer, J., Bruderer, S., et al. 2013, *A&A*, 550, A25
- González-Alfonso, E., Fischer, Aalto, S., & Falstad, N. 2014, *A&A*, 567, A91
- González-Alfonso, E., Fischer, J., Graciá-Carpio, J., et al. 2014b, *A&A*, 561, A27
- González-Alfonso, E., Fischer, J., Sturm, E., et al. 2015, *ApJ*, 800, 69
- González-Alfonso, E., Fischer, J., Spoon, H. W. W., et al. 2017, *ApJ*, 836, 11
- Harada, N., Herbst, E., & Wakelam, V. 2010, *ApJ*, 721, 1570
- Hopkins, P. F., Hernquist, L., Cox, T. J., & Kereš, D. 2008, *ApJS*, 175, 356
- Ichikawa, K., Ueda, J., Bae, H.-J., Kawamuro, T., Matsuoka, K., Toba, Y., & Shidatsu, M. 2019, *ApJ*, 870, 75
- Imanishi, M., Nakanishi, K., & Izumi, T. 2016a, *AJ*, 152, 218
- Imanishi, M., Nakanishi, K., & Izumi, T. 2016b, *ApJ*, 825, 44
- Ivezić, Ž., & Elitzur, M. 1997, *MNRAS*, 287, 799
- Ivezić, Ž., & Elitzur, M. 1999, *MNRAS*, 303, 864
- Lahuis, F., Spoon, H. W. W., Tielens, A. G. G. M., et al. 2007, *ApJ*, 659, 296
- Lusso, E., Comastri, A., Simmons, B. D., et al. 2012, *MNRAS*, 425, 623
- Martín, S., Aalto, S., Sakamoto, K., et al. 2016, *A&A*, 590, A25
- Mennella, V., Brucato, J. R., Colangeli, L., Palumbo, P., Rotundi, A., & Bussoletti, E. 1998, *ApJ*, 496, 1058
- Nomura, H., & Millar, T. J. 2004, *A&A*, 414, 409
- Planck Collaboration, 2011, *A&A*, 536, A25
- Richings, A. J., & Faucher-Giguère, C.-A. 2017, *MNRAS*
- Risaliti, G., & Elvis, M. 2004, *ASSL*, 308, 187
- Rolffs, R., Schilke, P., Wyrowski, F., Menten, K. M., Güsten, R., & Bisschop, S. E. 2011a, *A&A*, 527, A68
- Rolffs, R., Schilke, P., Wyrowski, F., Dullemond, C., Menten, K. M., Thorwirth, S., & Belloche, A. 2011b, *A&A*, 529, A76
- Rolffs, R., Schilke, P., Zhang, Q., & Zapata, L. 2011c, *A&A*, 536, A33
- Roth, N., Kasen, D., Hopkins, P. F., & Quataert, E. 2012, *ApJ*, 759, 36
- Rowan-Robinson, M., 1982, in “Submillimeter Astronomy”, eds. Phillips, P. & Beckman, J. Cambridge Univ. Press, pg. 47
- Sakamoto, K., Wang, J., Wiedner, M. C., et al. 2008, *ApJ*, 684, 957
- Sakamoto, K., Aalto, S., Wilner, D. J., et al. 2009, *ApJ*, 700, L104
- Sakamoto, K., Aalto, S., Evans, A. S., Wiedner, M. C., & Wilner, D. J. 2010, *ApJ*, 725, L228
- Sakamoto, K., Aalto, S., Costagliola, F., Martín, S., Ohyama, Y., Wiedner, M. C., & Wilner, D. J. 2013, *ApJ*, 764, 42
- Sakamoto, K., Aalto, S., Barcos-Muñoz, L., et al. 2017, *ApJ*, 849, 14
- Salter, C. J., Ghosh, T., Catinella, B., Lebron, M., Lerner, M. S., Minchin, R., & Momjian, E. 2008, *AJ*, 136, 389
- Salpeter, E. E. 1955, *ApJ*, 121, 161
- Schawinski, K., Koss, M., Berney, S., & Sartori, L. F. 2015, *MNRAS*, 451, 2517
- Scoville, N., Yun, M. S., & Bryant, P. M. 1997, *ApJ*, 484, 702
- Scoville, N. 2003, *Journal of Korean Astronomical Society*, 36, 167
- Scoville, N., Murchikova, L., Walter, F., et al. 2017, *ApJ*, 836, 66
- Soifer, B. T., Neugebauer, G., Matthews, K., et al. 2000, *AJ*, 119, 509
- Thorwirth, S., Wyrowski, F., Schilke, P., Menten, K. M., Brünken, S., Müller, H. S. P., & Winnewisser, G. *ApJ*, 586, 338
- Varenus, E., Conway, J. E., Martí-Vidal, I., Aalto, S., Beswick, R., Costagliola, F., & Klöckner, H.-R. 2014, *A&A*, 566, A15
- Wilner, D. J., De Pree, C. G., Welch, W. J., & Goss, W. M. 2001, *ApJ*, 550, L81
- Wilson, C. D., Rangwala, N., Glenn, J., Maloney, P. R., Spinoglio, L., & Pereira-Santaella, M. 2014, *ApJ*, 789, L36

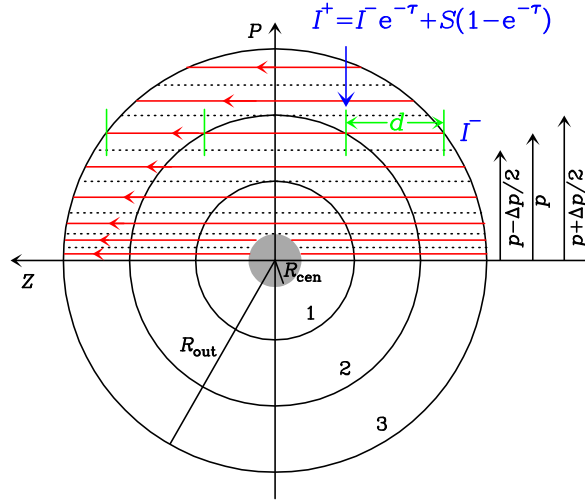


Figure 14. Sketch of the modeled source. The radiation field is simulated by means of parallel rays (in red), each one representing the intensity in an interval $[p - \Delta p/2, p + \Delta p/2]$. After crossing a shell, the intensity is updated according to eq. (A2). These rays are used to compute the cooling and heating of every shell (eqs. A5 and A6), as well as the emergent SED and the radiation pressure on dust.

APPENDIX

A. THE DUST TEMPERATURE PROFILE

A.1. The basic approach

Figure 14 shows an schematic approach of the modeled source. The source is divided into a number N_{sh} of spherical shells, within which all physical parameters are uniform. The basic assumption of the approach to calculate the dust temperature profile is that the radiation from the heating source(s) is *locally* absorbed by dust and re-emitted in the infrared. For AGN models, a central compact blackbody source with temperature $T_{\text{cen}} = 1300$ K is assumed to re-radiate the AGN luminosity $L_{\text{IR}}^{\text{cen}}$, with radius R_{cen} :

$$L_{\text{IR}}^{\text{cen}} = 4\pi R_{\text{cen}}^2 \sigma T_{\text{cen}}^4 \quad (\text{A1})$$

For SB models, we assume that the energy deposited (and absorbed) per unit time in shell m is proportional to both the dust mass and the density of that shell, $\Gamma_m^{\text{SB}} \propto \rho_m M_m$ (normalized as $L_{\text{IR}}^{\text{SB}} = \sum_m \Gamma_m^{\text{SB}}$), and re-emitted at the equilibrium dust temperature of the shell. The approximation that the bulk of the dust is heated by the *mid- and far-infrared radiation field* within the source enables us to neglect scattering.

Owing to the spherical symmetry of the source, the radiation field is simulated by means of a set of parallel “rays” that cross the source, each one characterized by an impact parameter p and simulating the intensity between $p - \Delta p/2$ and $p + \Delta p/2$ in a number of frequency intervals. When crossing shell m , the intensity of the ray in each frequency interval is updated as

$$I_{p,m,\nu}^+ = I_{p,m,\nu}^- \exp\{-\tau_{p,m,\nu}\} + S_{m,\nu} (1 - \exp\{-\tau_{p,m,\nu}\}), \quad (\text{A2})$$

where $I_{p,m,\nu}^-$ and $I_{p,m,\nu}^+$ are the incident and emergent intensities, $S_{m,\nu}$ is the source function, and $\tau_{p,m,\nu}$ is the optical depth of the ray through shell m at frequency ν :

$$S_{m,\nu} = \frac{2h\nu^3}{c^2} \frac{1}{\exp\{\frac{h\nu}{kT_m}\} - 1} \quad (\text{A3})$$

$$\tau_{p,m,\nu} = \rho_m \kappa_\nu d_{p,m}. \quad (\text{A4})$$

In the above equations, T_m is the dust temperature in shell m , ρ_m is the density of dust, κ_ν is the mass absorption coefficient of dust at frequency ν , and $d_{p,m}$ is the length of the path travelled by the ray in shell m . For rays crossing the central source, the intensity of the ray is updated correspondingly.

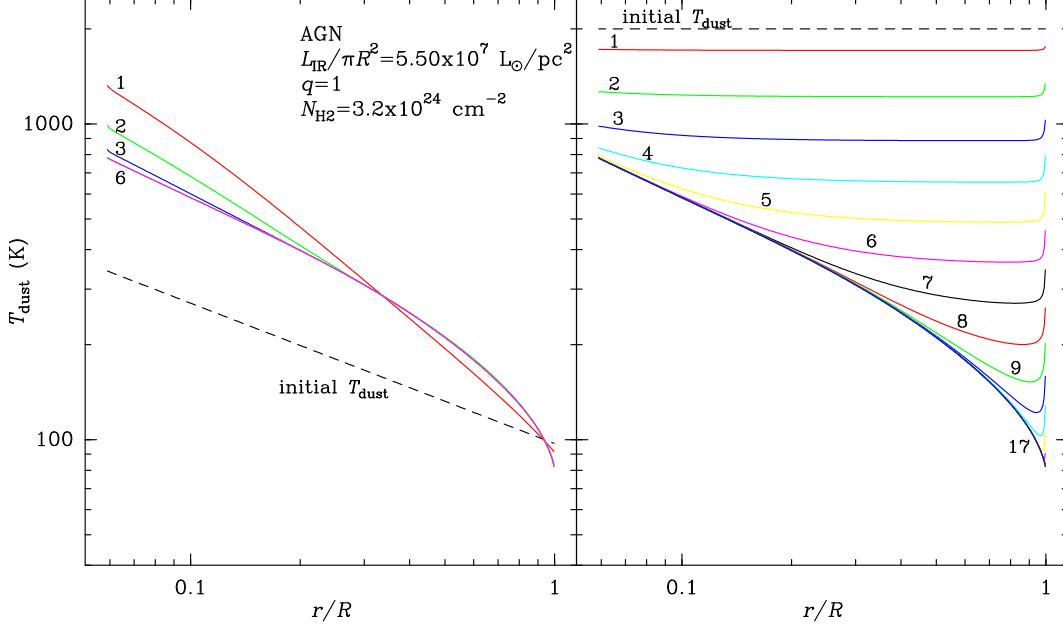


Figure 15. Example of convergence of our models. The two panels show with coloured curves the computed T_{dust} after each iteration (labeled with the iteration number), for the same model parameters but different initial temperatures. In the left panel, the initial T_{dust} were close to the optically thin solution, while T_{dust} was taken to be the (unphysical) value of 2000 K in the right-hand panel to check for possible local minima (dashed curves). The final T_{dust} profile, attained after 6 and 17 iterations in the left-hand and right-hand panels, is the same in both calculation. Since the first iteration of the Newton-Raphson approach usually overestimates the T_{dust} -correction, $0.5 \times \Delta T_{\text{dust}}$ was used in the first iteration.

Similar to the method used for lines and described in [González-Alfonso & Cernicharo \(1997\)](#), an integral approach is used to compute the heating and cooling of dust in any shell. The cooling of dust grains in shell m is given by

$$\Lambda_m = 8\pi^2 \int d\nu \int_0^{R_m} dp p S_{m,\nu} (1 - \exp\{-\tau_{p,m,\nu}\}), \quad (\text{A5})$$

where R_m is the outer radius of shell m . Similarly, the heating of dust grains in shell m is

$$\Gamma_m = 8\pi^2 \int d\nu \int_0^{R_m} dp p I_{p,m,\nu} \exp\{-\tau_{p,m,\nu}\} + \Gamma_m^{\text{SB}}, \quad (\text{A6})$$

and the equilibrium dust temperatures are found through an iterative method by equalizing the cooling and heating in all shells:

$$\Gamma_m - \Lambda_m = 0. \quad (\text{A7})$$

The integrals in eqs. (A5) and (A6) are calculated by using the rays that simulate the radiation field. These same rays are also used to compute the emergent spectral energy distribution (SED) and the radiation pressure on dust (see below), ensuring the overall consistency of the method. In all our models, energy is conserved to better than 1%.

A.2. Convergence

Equation A7 is solved iteratively, starting with the T_{dust} profile of either the optically thin solution or of the solution of another model. In each iteration, the full Jacobian matrix is computed as the rays cross the source, and a Newton-Raphson procedure calculates the correction ΔT_{dust} in all shells. The convergence criterion is that the relative variation of temperatures, $\Delta T_{\text{dust}}/T_{\text{dust}}$, is lower than 10^{-4} in all shells.

No local minimum was found in our approach, and the same equilibrium T_{dust} profile was obtained regardless of the initial temperatures (see Fig. 15). When starting with the optically thin solution, convergence was achieved in 5–8 iterations even in the most optically thick models.

Although the model implicitly conserves energy (i.e. L_{IR} calculated from the emergent SED is equal to $L_{\text{IR}}^{\text{cen}}$ in case of an AGN model, or $L_{\text{IR}}^{\text{SB}}$ in case of a SB model), and eq. (A7) is accomplished in every shell, accurate T_{dust} profiles are only obtained

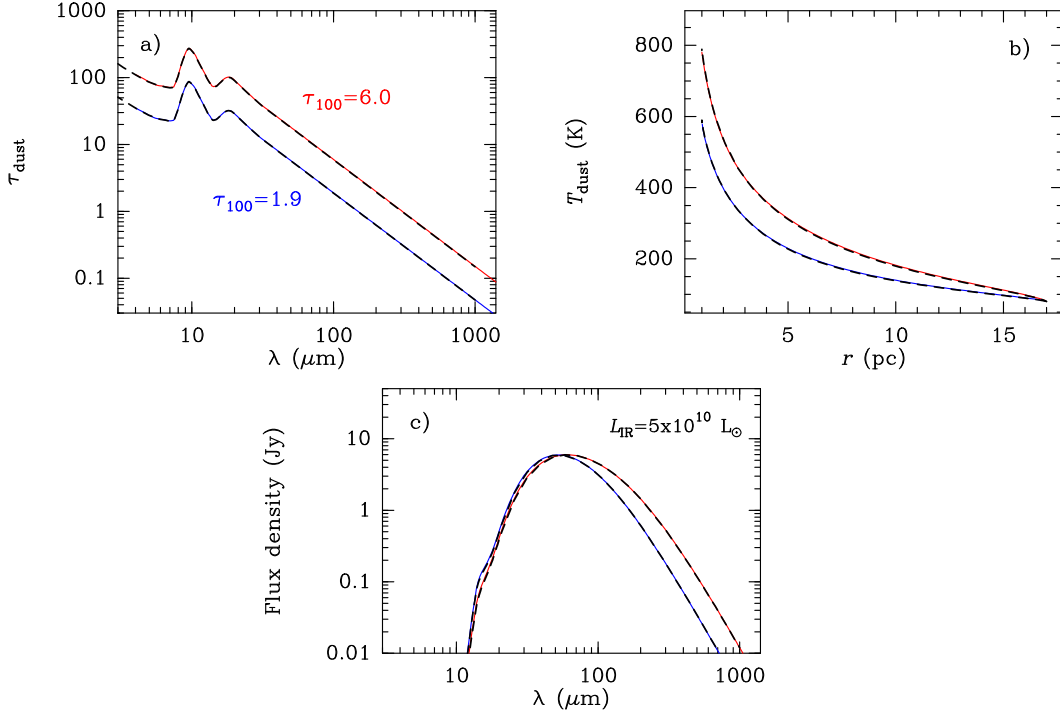


Figure 16. Comparison between the results of two of our models (coloured curves) and those obtain with the V4 version of the code DUSTY (Ivezić & Elitzur 1997, 1999) (dashed black lines). The models are both optically thick (panel a), and the heating source is punctual with a luminosity of $5 \times 10^{10} L_{\odot}$ observed at 59.1 Mpc. These calculations use the red κ_{ν} -curve of Fig. 1. As shown in panels b and c, results from both codes are indistinguishable.

if a sufficiently fine grid is used. The condition of convergence to a unique (exact) solution is that every shell is optically thin at all wavelengths involved in the absorption and emission. The optical depth at the peak of the $10 \mu\text{m}$ silicate feature is lower than 1 for $N_{\text{H}_2} < 10^{22} \text{ cm}^{-2}$, and this constraint was used to establish the maximum thickness of every shell in all our models, with a minimum number of shells of 100 to describe properly the T_{dust} profile. In models with the maximum $N_{\text{H}_2} = 10^{25} \text{ cm}^{-2}$, the number of shells was ≈ 1000 .

A.3. Test

The code was benchmarked in two optically thick models with the version V4 of the code DUSTY (Ivezić & Elitzur 1997, 1999), yielding indistinguishable T_{dust} profiles and emergent SEDs (Fig. 16). In both comparison models, the heating source is assumed to be punctual (i.e. our AGN models).

A.4. Radiation pressure

Radiation pressure on dust is accurately calculated by using the same rays that simulate the radiation field (Fig. 14). As a ray with impact parameter p is crossing the source toward the interior (i.e. for $z < 0$ in Fig. 14), the radiation exerts an inward pressure; the net inward force on shell m is given by

$$F_m^{\text{inward}} = \frac{8\pi^2}{c} \int d\nu \int_0^{R_m} dp p \cos \theta I_{p,m,\nu} (1 - \exp\{-\tau_{p,m,\nu}\}), \quad (\text{A8})$$

where $\cos \theta = \sqrt{1 - (p/r)^2}$ corrects for the radial component. Likewise, when the ray is crossing the source toward the outside (for $z > 0$ in Fig. 14), the net outward force on shell m due to radiation pressure has the same expression:

$$F_m^{\text{outward}} = \frac{8\pi^2}{c} \int d\nu \int_0^{R_m} dp p \cos \theta I_{p,m,\nu}^- (1 - \exp\{-\tau_{p,m,\nu}\}), \quad (\text{A9})$$

The net (outward) force on shell m is the difference between both, $F_m^{\text{outward}} - F_m^{\text{inward}}$.

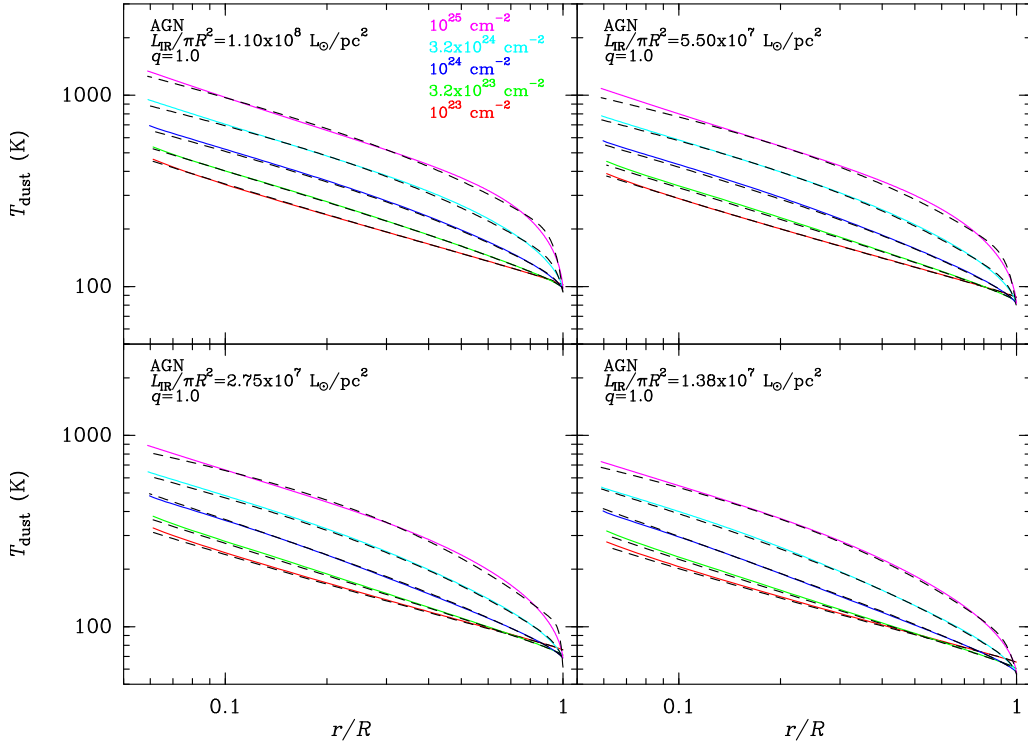


Figure 17. The T_{dust} profiles for AGN models with $q = 1.0$ ($\rho \sim r^{-q}$). Each panel shows results for fixed $L_{\text{IR}}/\pi R^2$ and different H_2 column densities (as indicated in the upper-left panel). The calculations use the red κ_ν -curve of Fig. 1. The dashed black curves indicate the fits to the T_{dust} profiles using eq. (A10), with parameters listed in Tables 3 and 4.

A.5. Overall results and fitting

The T_{dust} profiles as a function of the normalized radius $r_n \equiv r/R$ depend on the spatial distribution of the heating source(s) (AGN or SB), the surface brightness (characterized as $L_{\text{IR}}/(\pi R^2)$), the density profile ($\rho \sim r^{-q}$), the column density (characterized as N_{H_2} by assuming a gas-to-dust ratio of 100 by mass), and only very slightly on the κ_ν -curve of Fig. 1. Results can then be easily scaled to any size R . A subset of T_{dust} profiles is shown in Figs. 17-20. Each curve has been fitted to a modified Schechter function:

$$\log_{10} T_{\text{dust}} = A r_n^\alpha \exp\{-\beta r_n\} \frac{1}{1 + b r_n^\gamma}, \quad (\text{A10})$$

where the last factor $(1 + b r_n^\gamma)^{-1}$ is included to approximately account for the sharp decrease of T_{dust} close to the surface for high N_{H_2} . For each model, the 5 parameters A , α , β , b , and γ are fitted to minimize χ^2 , and their values are listed in Tables 3 (AGN models) and 4 (SB models). Eq. A10 gives T_{dust} accurate to better than 13% for all models at all radii.

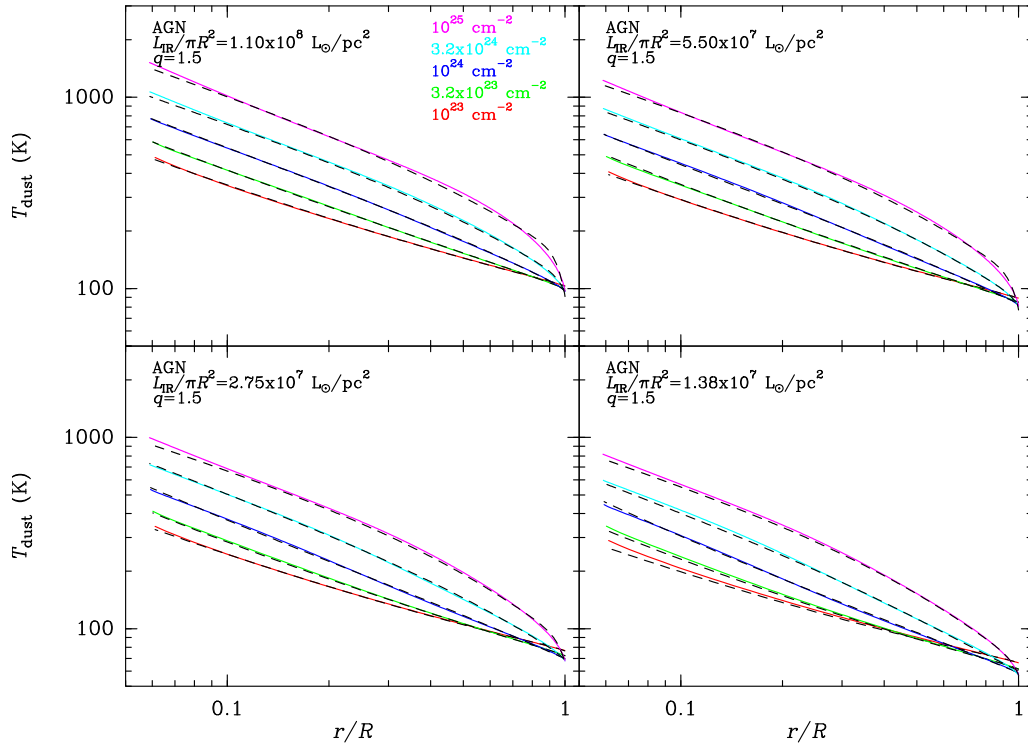


Figure 18. Same as Fig. 17 but for AGN models with $q = 1.5$.

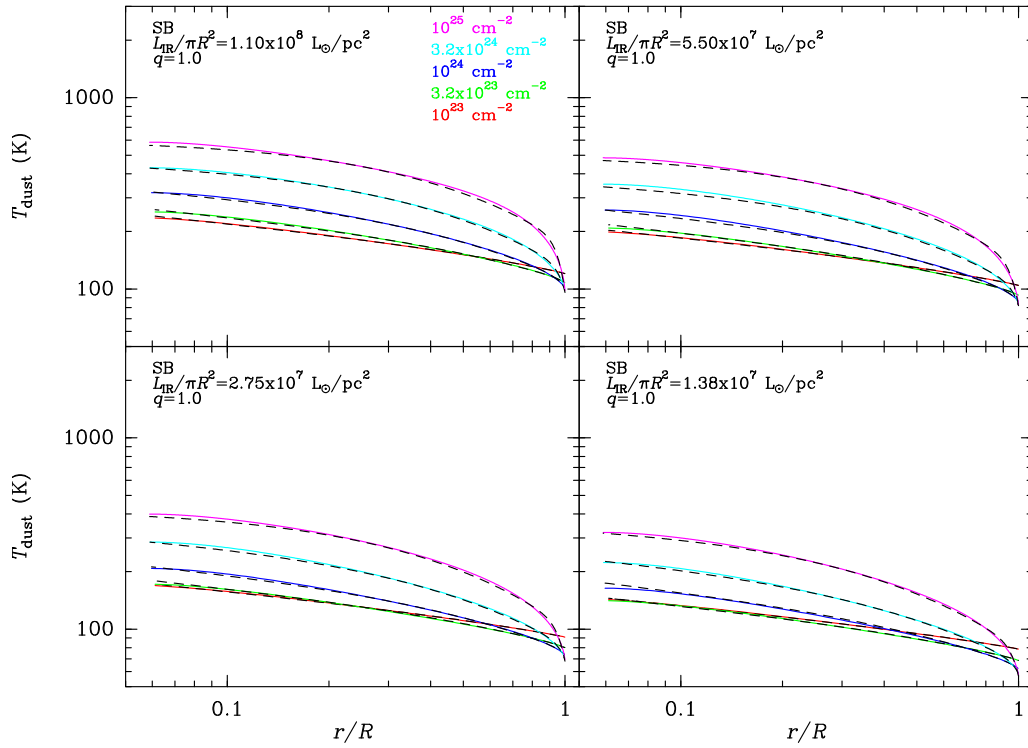


Figure 19. Same as Fig. 17 but for SB models with $q = 1.0$.

Table 3. Fitting values for the T_{dust} profiles of AGN models

Type	$L_{\text{IR}}/\pi R^2$ ($10^7 L_{\odot}/\text{pc}^{-2}$)	N_{H_2} (10^{24} cm^{-2})	q	A	α (10^{-2})	β (10^{-2})	b (10^{-3})	γ
AGN	11.01	10.00	1.0	2.668	-5.648	16.764	146.265	20.773
AGN	11.01	10.00	1.5	2.536	-8.024	15.725	107.428	20.365
AGN	11.01	3.16	1.0	2.549	-5.516	18.780	74.416	20.608
AGN	11.01	3.16	1.5	2.404	-8.210	16.134	35.358	20.576
AGN	11.01	1.00	1.0	2.362	-6.579	15.215	24.373	20.647
AGN	11.01	1.00	1.5	2.213	-9.659	10.109	6.375	21.118
AGN	11.01	0.32	1.0	2.172	-8.233	7.812	8.106	20.747
AGN	11.01	0.32	1.5	2.062	-10.521	2.918	2.187	20.036
AGN	11.01	0.10	1.0	2.062	-9.089	2.173	4.829	20.271
AGN	11.01	0.10	1.5	2.000	-10.362	-0.941	3.613	21.048
AGN	5.51	10.00	1.0	2.635	-4.868	20.881	132.058	20.962
AGN	5.51	10.00	1.5	2.497	-7.637	19.768	86.143	20.481
AGN	5.51	3.16	1.0	2.472	-5.739	20.961	56.616	20.667
AGN	5.51	3.16	1.5	2.321	-8.561	17.684	20.085	20.665
AGN	5.51	1.00	1.0	2.243	-7.443	14.488	16.834	21.090
AGN	5.51	1.00	1.5	2.112	-10.263	9.888	-4.572	5.112
AGN	5.51	0.32	1.0	2.067	-8.844	6.632	6.585	21.918
AGN	5.51	0.32	1.5	1.964	-11.304	1.615	2.226	16.081
AGN	5.51	0.10	1.0	1.987	-9.366	1.819	4.110	22.515
AGN	5.51	0.10	1.5	1.929	-10.606	-1.348	3.617	23.493
AGN	2.75	10.00	1.0	2.632	-4.143	27.796	122.975	59.449
AGN	2.75	10.00	1.5	2.438	-7.393	23.311	60.730	20.678
AGN	2.75	3.16	1.0	2.360	-6.356	21.630	40.503	21.179
AGN	2.75	3.16	1.5	2.209	-9.538	17.708	7.453	20.403
AGN	2.75	1.00	1.0	2.109	-8.964	12.675	11.949	19.999
AGN	2.75	1.00	1.5	1.977	-11.668	7.044	-0.686	14.677
AGN	2.75	0.32	1.0	1.963	-9.598	5.346	5.772	22.366
AGN	2.75	0.32	1.5	1.870	-11.813	0.308	3.141	24.129
AGN	2.75	0.10	1.0	1.912	-9.521	1.432	3.826	23.814
AGN	2.75	0.10	1.5	1.858	-10.858	-1.793	4.020	22.600
AGN	1.38	10.00	1.0	2.492	-5.092	27.027	88.262	20.165
AGN	1.38	10.00	1.5	2.346	-7.865	25.433	36.323	21.058
AGN	1.38	3.16	1.0	2.217	-7.653	20.534	29.480	23.640
AGN	1.38	3.16	1.5	2.167	-9.127	28.203	-81.325	1.851
AGN	1.38	1.00	1.0	1.972	-10.267	10.214	9.855	19.857
AGN	1.38	1.00	1.5	1.848	-13.036	4.253	1.653	29.131
AGN	1.38	0.32	1.0	1.865	-10.261	4.148	5.259	22.840
AGN	1.38	0.32	1.5	1.780	-12.280	-0.887	4.103	23.617
AGN	1.38	0.10	1.0	1.840	-9.805	1.112	3.797	24.068
AGN	1.38	0.10	1.5	1.790	-10.765	-2.100	4.491	24.373

Table 4. Fitting values for the T_{dust} profiles of SB models

Type	$L_{\text{IR}}/\pi R^2$ ($10^7 L_{\odot}/\text{pc}^{-2}$)	N_{H_2} (10^{24} cm^{-2})	q	A	α (10^{-2})	β (10^{-2})	b (10^{-3})	γ
SB	11.01	10.00	1.0	2.797	0.121	22.374	130.334	21.680
SB	11.01	10.00	1.5	2.720	-3.202	24.087	82.954	20.418
SB	11.01	3.16	1.0	2.618	-0.645	21.688	62.731	20.498
SB	11.01	3.16	1.5	2.545	-3.968	22.564	20.155	20.297
SB	11.01	1.00	1.0	2.395	-1.965	15.750	22.036	20.438
SB	11.01	1.00	1.5	2.317	-5.408	14.695	-4.138	10.549
SB	11.01	0.32	1.0	2.238	-2.919	8.951	6.767	20.822
SB	11.01	0.32	1.5	2.161	-6.360	6.618	-2.733	16.831
SB	11.01	0.10	1.0	2.183	-3.206	4.703	1.186	20.121
SB	11.01	0.10	1.5	2.131	-6.014	3.170	-2.224	17.758
SB	5.51	10.00	1.0	2.719	0.106	24.519	114.998	19.086
SB	5.51	10.00	1.5	2.662	-2.907	27.382	62.878	20.524
SB	5.51	3.16	1.0	2.499	-0.954	21.858	50.524	20.844
SB	5.51	3.16	1.5	2.435	-4.563	22.907	7.946	20.478
SB	5.51	1.00	1.0	2.272	-2.439	14.470	17.347	20.906
SB	5.51	1.00	1.5	2.191	-6.121	12.841	-4.981	13.836
SB	5.51	0.32	1.0	2.144	-3.252	8.074	5.220	20.903
SB	5.51	0.32	1.5	2.070	-6.570	5.652	-3.198	13.056
SB	5.51	0.10	1.0	2.109	-3.313	4.279	0.685	19.337
SB	5.51	0.10	1.5	2.062	-5.912	2.906	-2.423	15.023
SB	2.75	10.00	1.0	2.623	-0.097	26.483	99.361	20.078
SB	2.75	10.00	1.5	2.574	-3.269	29.718	40.817	20.673
SB	2.75	3.16	1.0	2.362	-1.805	20.969	40.583	21.209
SB	2.75	3.16	1.5	2.302	-5.386	22.021	-4.402	13.334
SB	2.75	1.00	1.0	2.154	-3.001	13.147	13.297	20.580
SB	2.75	1.00	1.5	2.068	-7.087	10.838	-5.477	15.250
SB	2.75	0.32	1.0	2.055	-3.449	7.298	3.832	21.804
SB	2.75	0.32	1.5	1.985	-6.839	4.832	-3.067	13.045
SB	2.75	0.10	1.0	2.037	-3.407	3.878	0.396	22.058
SB	2.75	0.10	1.5	1.995	-5.954	2.675	-2.425	14.561
SB	1.38	10.00	1.0	2.482	-0.833	26.809	83.318	20.178
SB	1.38	10.00	1.5	2.439	-4.281	30.295	19.625	19.119
SB	1.38	3.16	1.0	2.215	-2.575	19.540	32.295	22.092
SB	1.38	3.16	1.5	2.139	-6.685	19.307	-7.106	16.969
SB	1.38	1.00	1.0	2.038	-3.623	11.836	9.638	19.448
SB	1.38	1.00	1.5	1.949	-7.759	8.939	-5.580	15.256
SB	1.38	0.32	1.0	1.965	-3.550	6.545	2.644	24.918
SB	1.38	0.32	1.5	1.903	-6.949	4.278	-3.154	12.858
SB	1.38	0.10	1.0	1.964	-3.517	3.486	0.530	81.436
SB	1.38	0.10	1.5	1.927	-5.970	2.527	-2.399	14.011

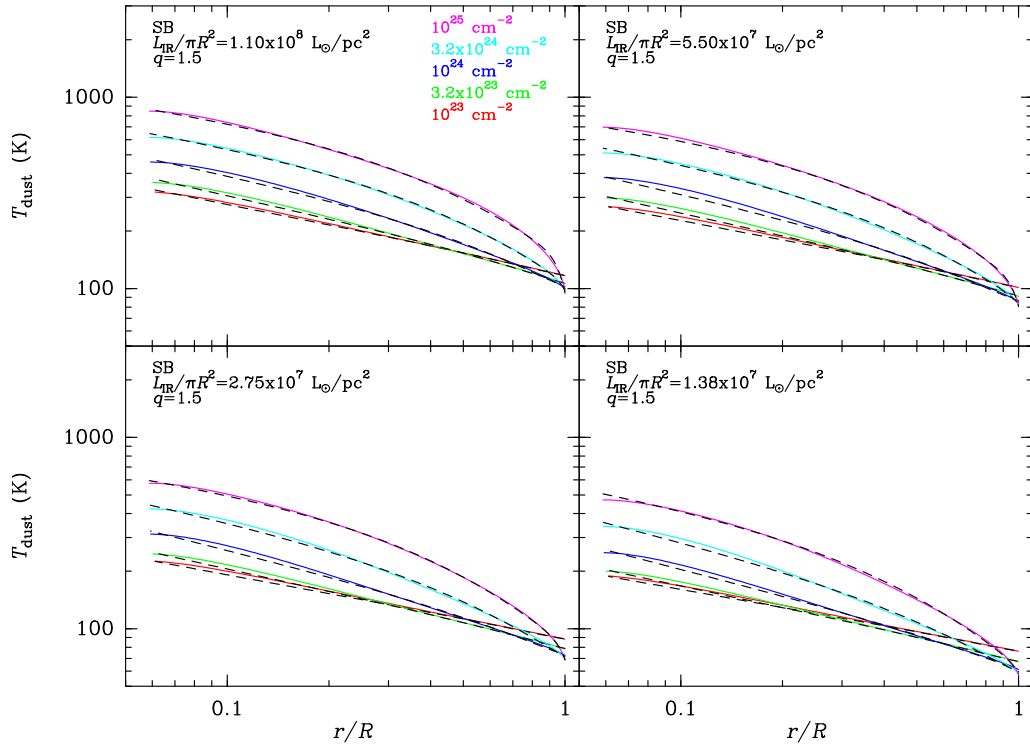


Figure 20. Same as Fig. 17 but for SB models with $q = 1.5$.